Check for updates

Behaviorome profiling of anti-tumor and pro-tumor human neutrophil subtypes in a microphysiological system

Shuai Shao, [iD] [ab] Daniel Duncko [iD] [a] and Caroline N. Jones [iD] *[ab]

Neutrophils exhibit a paradoxical role in cancer, either combating the tumor or facilitating its progression. Studies in mice have shown that polarizing neutrophils from a pro-tumor "N2" phenotype to an anti-tumor "N1" phenotype can serve as a strategy for immunotherapy. Understanding the behavioral differences between N1 and N2 human neutrophil subtypes in the solid tumor tissue is important for developing novel cancer immunotherapy. However, it is challenging to monitor neutrophil–cancer interactions in the human tumor tissue. In this study, we developed a human cell-based microphysiological system to quantify both real-time and end-point behaviors of N1-like and N2-like neutrophils during their interactions with pancreatic cancer in a 3D collagen matrix. We first validated that N1-like neutrophils showed higher levels of pro-inflammatory hallmarks including ROS production, IL-8 secretion, and NET release and 2D cancer cytotoxicity than N2-like neutrophils. We found that N2-like neutrophils showed greater migration to cancer cells and higher motility after migration than N1-like neutrophils. N1-like neutrophils engaged in longer contact with tumor spheroids and infiltrated greater into tumor spheroids than N2-like neutrophils. N1-like neutrophils also attenuated the progression of tumor spheroids in terms of invasion, proliferation (Ki-67 expression), and epithelial–mesenchymal transition (vimentin expression) compared to N2-like neutrophils, although tumor apoptosis was not affected. Our microphysiological system reveals the distinct "behavioromes" of anti-tumor and pro-tumor human neutrophil subtypes in pancreatic cancer, which may inform the design and development of novel cancer immunotherapies aiming to modulate specific neutrophil behaviors.

Introduction

The immune system is a double-edged sword in cancer and can either inhibit or promote tumor progression.[1] Neutrophils are the most abundant immune cells in human blood and the first line of defense against microbial infection, where they fight invading pathogens using a variety of cytotoxic mechanisms.[2–5] However, neutrophils can also get recruited by cancer cells into the solid tumor tissue and promote tumor progression.[2,6–13] Neutrophils have been reported to promote proliferation, angiogenesis, and metastasis of solid tumors, thereby subverting the canonical role of neutrophils to protect the body from harm.[2,6–13] Both high neutrophil-to-lymphocyte ratio in peripheral blood and high neutrophil infiltration in tumor correlate with poor prognosis and worse responses to chemotherapy, radiotherapy, and T cell-based immunotherapy

in human patients of various cancer types.[2,3,14] Neutrophils have been recently explored as a novel promising therapeutic target for cancer in different ways. One approach is to unleash the cytotoxic potential of neutrophils to kill cancer cells.[2] Early studies in mice show that blockade of transforming growth factor-β (TGF-β) leads to the recruitment of antitumor, cytotoxic neutrophils into the tumor and reduces tumor growth.[15] Similarly, other studies in mice found that interferon-β (IFN-β) can also polarize neutrophils toward the antitumor phenotype and slow down tumor growth.[16–18] These murine models have shown that neutrophils can be modulated by molecular cues to exhibit either an anti-tumor (denoted as "N1") or a pro-tumor (denoted as "N2") phenotype.[19–21] This functional plasticity suggests the polarization of neutrophils toward an anti-tumor "N1" phenotype to be a potential therapeutic strategy.[22]

Most studies on polarization of neutrophils to date rely on murine models.[19–21] Translation of neutrophil-targeting immunotherapy from murine models to cancer patients is particularly challenging due to many differences between mouse and human neutrophils.[20] Despite recent attempts to polarize human neutrophils toward N1 and N2 states *in vitro*,[19,23–26] it remains elusive how N1 and N2 human

a Department of Bioengineering, The University of Texas at Dallas, Richardson, TX, 75080, USA. E-mail: caroline.jones@utdallas.edu

b Department of Biomedical Engineering, UT Southwestern Medical Center, Dallas, TX, 75235, USA

neutrophils behave in the tumor tissue, interact with cancer cells, and influence tumor progression differently.[11,19,20] Moreover, it has not been studied in the preclinical stage as to whether N1 polarization of neutrophils could potentially serve as a therapy for human cancer.[11,19,20] These knowledge gaps exist partially due to the difficulty using traditional *in vitro* and *in vivo* models to tease out and measure specific immune cell–cancer interactions in the highly complex and heterogeneous tumor microenvironment of the human body. Microphysiological systems, including organ-on-a-chip systems, have emerged as novel *in vitro* models for investigating immune cell–cancer interactions and for the evaluation of immunotherapies.[8,27–33] These systems are more physiologically relevant than traditional *in vitro* models by combining microfluidic technology with 3D cell culture and tissue engineering to recapitulate key aspects of the tumor microenvironment with precise spatial control and compartmentalization of different cell types.[8,27–29,34,35] Moreover, in contrast to most *in vivo* animal models, these systems easily allow the use of human cells and enable direct

visualization and quantification of cellular behaviors and interactions with single-cell resolution in real time.[36,37] As a result, microphysiological systems have been utilized to study neutrophil–cancer interactions using human cells in the recent six years.[38–49] Some examined neutrophil recruitment to the primary tumor site,[38,39,45–49] while others examined the effect of circulating neutrophils on cancer cell extravasation and metastasis at the secondary site.[41–44] Most of these studies performed end-point measurements such as neutrophil infiltration in tumor, tumor invasion, and release of neutrophil extracellular traps (NETs) and missed the temporal dynamics of neutrophil–tumor interactions in real time. Moreover, none of these studies examined different subtypes of neutrophils such as N1 and N2 neutrophils. Other researchers have developed microsystems to quantify the temporal dynamics of interactions between cancer and other immune cell types such as T cells in real time,[50–58] including immune cell motility (velocity and directionality), kinetics of contact with cancer cells, infiltration into tumor, and cancer cell apoptosis. However, these studies did not
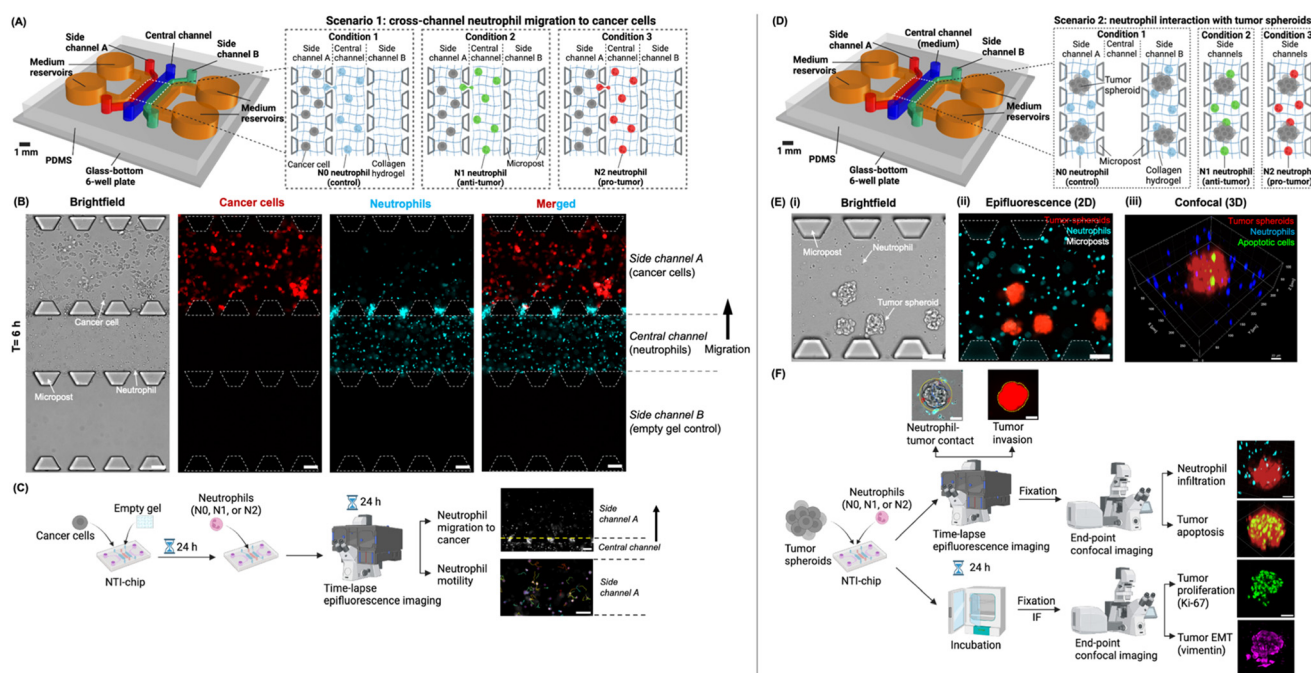

Fig. 1 Experimental design of the "neutrophil–tumor interactions on-a-chip" (NTI-chip) microphysiological system in two independent scenarios. (A) In scenario 1, the NTI-chip models the migration of different human neutrophil subtypes (*i.e.*, N0, N1, or N2 neutrophils) from the central channel into side channel A housing cancer cells, thus achieving spatial compartmentalization. Both neutrophils and cancer cells were embedded in 3D collagen hydrogel to mimic the extracellular matrix of the tumor tissue. Side channel B housed empty hydrogel, acting as a negative control for neutrophil migration. Created with Rhino 7 and **https://BioRender.com**. (B) Representative 10× brightfield and epifluorescence images showing neutrophils (blue) migrating from the central channel into side channel A housing cancer cells (red) on the NTI-chip at *t* = 6 h as a representative time point. Scale bar, 100 μm. (C) The workflow of a typical experiment for scenario 1. Neutrophil migration into side channel A and neutrophil motility after migration into side channel A were quantified as readouts. Created with **https://BioRender.com**. (D) In scenario 2, the NTI-chip models the interaction of N0, N1, or N2 neutrophils with tumor spheroids embedded in 3D collagen hydrogel, which mimics the solid tumor tissue. Side channels A and B are technical replicates. Created with Rhino 7 and **https://BioRender.com**. (E) Representative 10× brightfield (i) and epifluorescence images (ii) and 3D rendering of 10× confocal images (iii) showing neutrophils (blue) and tumor spheroids (red) in the side channels of the NTI-chip. Apoptotic cells were stained with Caspase-3/7 Green. Scale bar, 100 μm in (ii). *X*–*y*–*z* coordinates are shown around the field of view in (iii). (F) The workflow of a typical experiment for scenario 2 and the behaviors of neutrophils and tumor spheroids that were quantified as readouts. IF, immunofluorescence. EMT, epithelial–mesenchymal transition. Created with **https://BioRender.com**.

focus on neutrophils; nor did they examine other aspects of tumor progression than apoptosis such as invasion, proliferation, and epithelial–mesenchymal transition (EMT) which is known as an early sign of metastasis.[59,60] A comprehensive study that integrates both real-time and end-point measurements to map the full "behaviorome" (*i.e.*, a collection of behaviors) of N1 and N2 neutrophils in solid tumor tissues could significantly advance our understanding of their complex roles in cancer progression and therapeutic potential.

In this study, we engineered a human cell-based microphysiological system termed "NTI-chip" (neutrophil–tumor interactions on-a-chip) to monitor and quantify the interactions of N1-like or N2-like human neutrophil subtypes with pancreatic cancer in both the individual cancer cell format and the tumor spheroid format in a 3D collagen matrix (Fig. 1). The NTI-chip enabled us to characterize the behavioral differences between N1-like and N2-like neutrophils in migration to cancer cells, motility, contact with tumor spheroids, and infiltration into tumor spheroids. The NTI-chip also allowed us to examine the reciprocal responses of tumor spheroids to the two neutrophil subtypes including apoptosis, invasion, proliferation, and EMT. We found that N2-like neutrophils showed greater migration to individual cancer cells and higher motility after migration than N1-like neutrophils. N1-like neutrophils engaged in longer contact with tumor spheroids and infiltrated greater into tumor spheroids than N2-like neutrophils. N1-like neutrophils also attenuated the progression of tumor spheroids in terms of invasion, proliferation (Ki-67 expression), and EMT (vimentin expression) compared to N2-like neutrophils, although tumor apoptosis was not affected. This study reveals the distinct behavioromes of human neutrophil subtypes in pancreatic cancer, which adds a valuable dimension to the existing multi-omics approach that dominates the field of immunology research. The NTI-chip developed in this study can also facilitate the translation of neutrophil-based immunotherapies into cancer patients by serving as a complementary tool to animal models for cellular mechanism studies and preclinical drug testing.

Results

Design and characterization of the NTI-chip

We developed a microphysiological system "NTI-chip" to model the interactions of different neutrophil subtypes with cancer cells in two independent scenarios. The NTI-chip comprised a central channel (blue), side channel A (red), side channel B (green), and two outermost medium channels, each having two medium reservoirs (orange) (Fig. 1A). The five parallel channels were compartmentalized and interconnected by regularly spaced trapezoidal microposts. In scenario 1, the central channel housed neutrophils and side channel A housed cancer cells to model neutrophil migration toward cancer (Fig. 1A). Pancreatic cancer cells and neutrophils were separately embedded in 3D hydrogel made of type I collagen, as type I

collagen is the major component of the extracellular matrix in pancreatic cancer.[61–63] Side channel B housed empty hydrogel without cancer cells, acting as a negative control. The two medium channels were filled with culture medium to keep the cells alive and prevent evaporation (Fig. 1A). Time-lapse imaging was performed to capture neutrophil migration from the central channel into side channel A housing cancer cells over 24 h and neutrophil motility inside side channel A in real time (Fig. 1B and C). In scenario 2, neutrophils were co-embedded together with pancreatic tumor spheroids in the same 3D collagen hydrogel and loaded into both side channels A and B to model neutrophil–tumor interactions in the solid tumor tissue (Fig. 1D). The two side channels served as technical duplicates in the same chip, creating the benefit of doubling the throughput or the number of data points collected per experiment.[64–66] The central channel was filled with culture medium in this scenario. Tumor spheroids were shown to be surrounded by neutrophils in the NTI-chip using brightfield, 2D epifluorescence, and 3D confocal microscopy (Fig. 1E and S1A). The experimental workflow was designed to capture neutrophil motility (velocity, directionality, and displacement), contact with tumor spheroids (frequency and duration), and tumor spheroid invasion in the gel matrix in real time during a 24 h live imaging session (Fig. 1F). The NTI-chip was fixed at 24 h to collect end-point measurements using confocal imaging including neutrophil–tumor infiltration, tumor spheroid apoptosis, and Ki-67 and vimentin expressions by tumor spheroids as markers of proliferation and EMT respectively[67–70] (Fig. 1F). To better mimic the 3D shape and structure of solid tumors *in vivo*,[71] we grew tumor spheroids which are 3D aggregates of cancer cells from the RFP-PANC-1 human pancreatic cancer cell line (abbreviated as PANC-1) before loading them into the two side channels of the NTI-chip in scenario 2. We visualized the spatial structure of tumor spheroids *via* immunofluorescence of F-actin to show the borders between individual cancer cells in the spheroid (Fig. S1B). We then validated the high viability of tumor spheroids after 24 h of culture in the NTI-chip (percentage of live volume = 99.73 ± 0.48%) (Fig. S1C). We characterized the frequency distributions of both the diameter and the number of spheroids loaded per channel. The mean diameter of tumor spheroids was 96.7 ± 17.6 μm ($n = 667$) and each side channel was loaded with an average of 9.0 ± 3.9 spheroids ($n = 191$) (Fig. S1D). We also confirmed the ability of tumor spheroids to secrete interleukin-8 (IL-8), a known chemoattractant for neutrophils[37,72] and the main chemokine released by the tumor tissue to recruit neutrophils *in vivo*[12,13] (Fig. S1E).

N1-like neutrophils show higher levels of pro-inflammatory hallmarks and 2D cancer cytotoxicity than N2-like neutrophils

In this study of N1 and N2 human neutrophils, we used the HL-60 human promyelocytic leukemia cell line that has been extensively characterized and is the most commonly used model for primary human neutrophils.[73,74] We first differentiated HL-
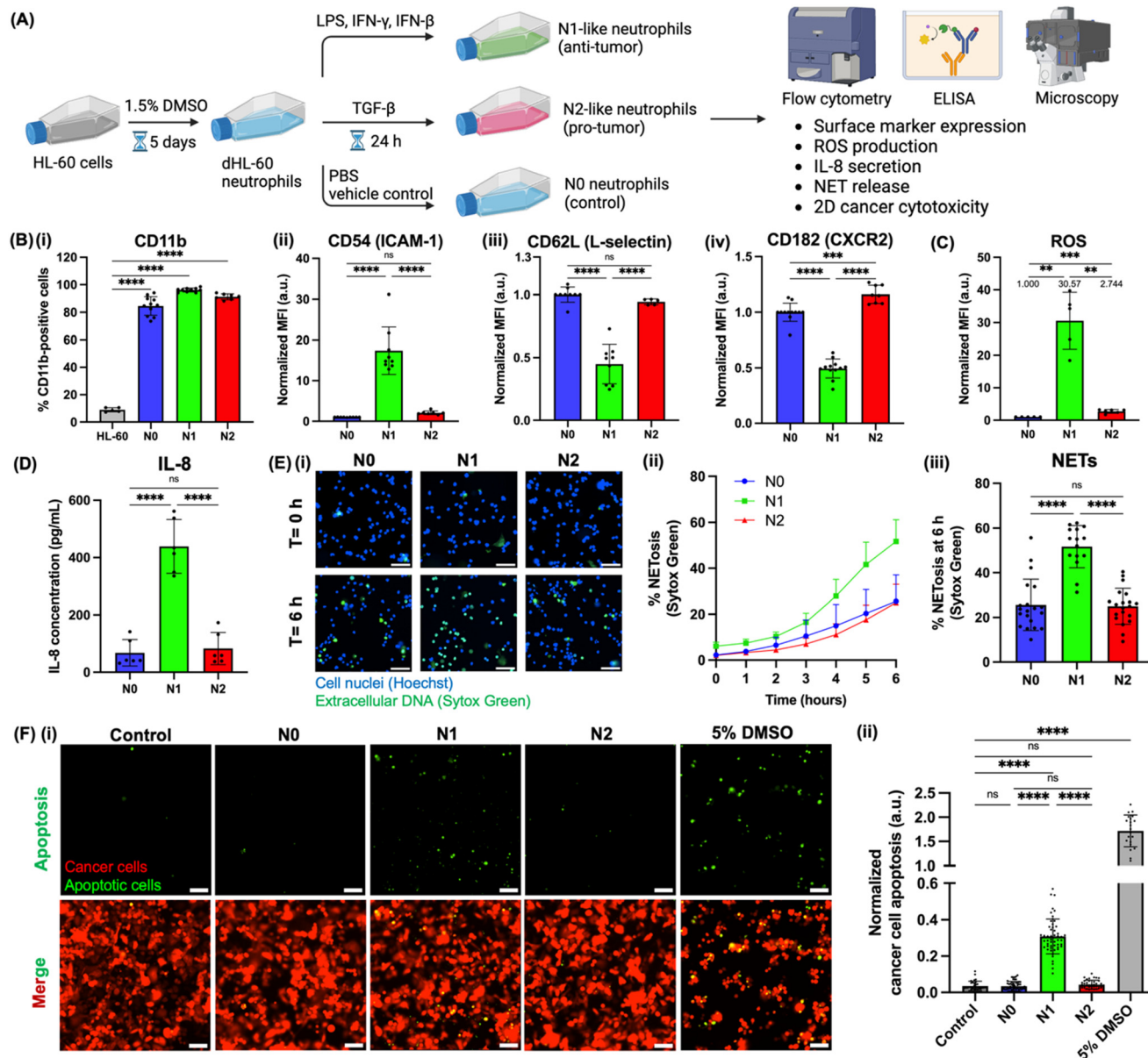
Fig. 2 Generation, validation, and characterization of N1-like and N2-like neutrophils. (A) HL-60 cells were differentiated with 1.5% DMSO for 5 days into a neutrophil-like state and polarized for 24 h with 100 ng mL^{-1} LPS, 50 ng mL^{-1} IFN-γ, and 50 ng mL^{-1} IFN-β towards an N1-like state or with 100 ng mL^{-1} TGF-β toward an N2-like state. The unpolarized control was denoted as N0 neutrophils. Created with https://BioRender.com. (B) Surface expression levels of general neutrophil marker CD11b (i) and N1/N2-related markers CD54 (ICAM-1) (ii), CD62L (L-selectin) (iii), and CD182 (CXCR2) (iv) by N0, N1-like, and N2-like neutrophils were examined using flow cytometry. CD11b expression by undifferentiated HL-60 cells was also examined as a negative control. MFI, median fluorescence intensity. Raw values in (ii)–(iv) were normalized by the mean of the N0 condition. (C) Phorbol myristate acetate (PMA)-induced reactive oxygen species (ROS) production by N0, N1-like, and N2-like neutrophils was assessed by flow cytometry. Raw values were normalized by the mean of the N0 condition. **: $p < 0.01$, ***: $p < 0.001$, three unpaired t tests between each pair. (D) IL-8 secretion by N0, N1-like, and N2-like neutrophils was assessed by ELISA. (E) (i) Representative 20× images showing the release of neutrophil extracellular traps (NETs) (Sytox Green, extracellular DNA) by N0, N1-like, and N2-like neutrophils (Hoechst blue, nuclei) induced by PMA on a 96-well plate at $t = 0$ h and 6 h. Scale bar, 50 μm. (ii) Temporal dynamics of PMA-induced NET release over 6 h. (iii) A bar plot showing the percentage of NET-releasing neutrophils at $t = 6$ h. Bars show mean ± SD of $n = 15$–20 random ROIs per condition. (F) N1-like neutrophils are cytotoxic against PANC-1 cancer cells. PANC-1 cancer cells in 2D monolayers were cultured alone (control), co-cultured with N0, N1-like, or N2-like neutrophils at a 1 : 20 ratio, or with 5% DMSO (positive control) for 24 h on a 96-well plate. (i) Representative 20× images showing PANC-1 cancer cells (red, RFP) and apoptotic cells (caspase-3/7 green) in specified conditions. Scale bar, 100 μm. (ii) Bar plot showing the normalized cancer cell apoptosis per ROI, defined by the ratio of the number of apoptotic cancer cells to the percentage of RFP fluorescence area of all cancer cells, in specified conditions. Apoptotic neutrophils were excluded from analysis by a size filter (<50 μm^2) in ImageJ. Each data point is an ROI and $n = 33$–54 random ROIs per condition. At least three independent experiments were performed. ns: ≥0.05, ****: $p < 0.0001$, ANOVA with Tukey multiple comparisons test.

60 cells into a neutrophil-like state denoted as dHL-60 neutrophils[73,75] and then polarized them into either a N1-like (anti-tumor) or a N2-like (pro-tumor) state as previously described[19,24,25] (Fig. 2A). The unpolarized control was denoted as N0 neutrophils, representing the naïve state.[19,20] Using the HL-60 cell line enabled us to perform stable N1 and N2 polarization *in vitro* for 24 h without worrying about the short life span (<24 h) and the loss of functionality of primary human neutrophils once isolated from peripheral blood.[20,73] We first confirmed the success of HL-60 differentiation by showing a significant upregulation of neutrophil surface marker CD11b[74,75] by N0, N1-like, and N2-like dHL-60 neutrophils (% CD11b-positive cells = 84.6%, 96.1%, and 91.3% respectively) compared to undifferentiated HL-60 cells (% CD11b-positive cells = 9.0%) ($p < 0.0001$) (Fig. 2Bi and S2A). We then validated the identity of our N1-like and N2-like neutrophils by showing that N1-like neutrophils were CD54^{high}/CD62L^{low}/CD182^{low} and

N2-like neutrophils were CD54^{low}/CD62L^{high}/CD182^{high} ($p < 0.0001$), which agrees with the expression patterns of typical N1 and N2 surface markers previously reported[2,19] (Fig. 2Bii–iv and S2B–D). We also validated using immunofluorescence that N1-like and N2-like neutrophils maintained their polarization states for at least 24 h in the NTI-chip (Fig. S3). We also found that N1-like neutrophils showed higher levels of pro-inflammatory hallmarks than N2-like neutrophils in terms of production of reactive oxygen species (ROS)[15,17] ($p < 0.01$), secretion of IL-8[76,77] ($p < 0.0001$), and release of NETs[17] ($p < 0.0001$) (Fig. 2C–E and S2E and S4). ROS production is also reported to be a direct cytotoxic mechanism employed by neutrophils.[2,20] Lastly, we found that N1-like neutrophils showed cytotoxicity against PANC-1 cancer cells in 2D monolayer co-cultures by inducing apoptosis ($p < 0.0001$) while N2-like and N0 neutrophils did not, thus validating the anti-tumor nature of N1-like neutrophils (Fig. 2F).
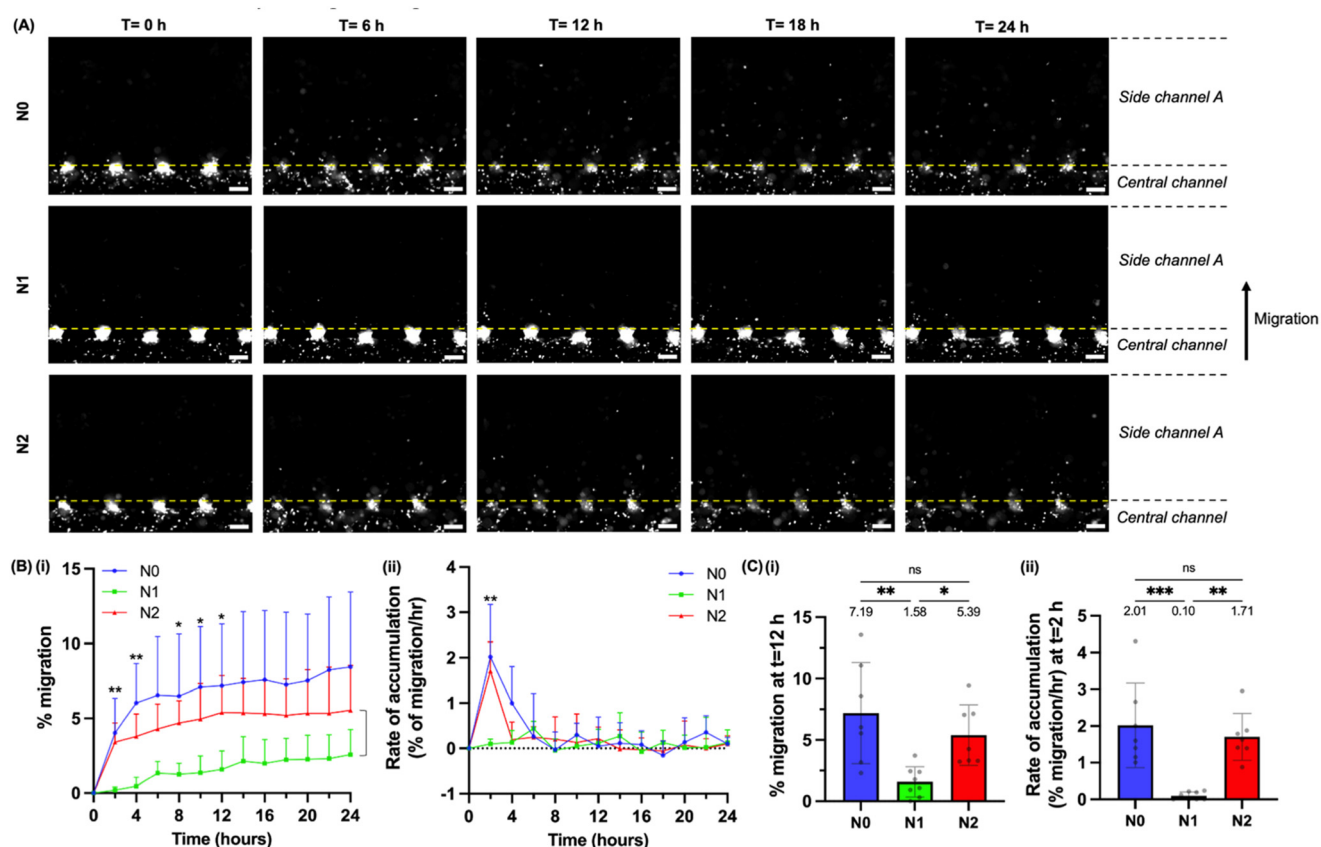

Fig. 3 In scenario 1, N2-like neutrophils show greater migration towards PANC-1 cancer cells than N1-like neutrophils. (A) Representative 10× images showing N0, N1-like, or N2-like neutrophils (white) migrating from the central channel into side channel A housing cancer cells (not shown) at $t = 0$ h, 6 h, 12 h, 18 h, and 24 h. The yellow dashed line marks the boundary between the central channel and side channel A. Scale bar, 100 μm. (B) Line graphs showing the percentage of neutrophil migration, defined as the number of neutrophils in side channel A at a given time point divided by the initial number of neutrophils in the central channel at $t = 0$ h (i), and the rate of neutrophil accumulation inside side channel A, defined as the increase in the percentage of neutrophil migration per hour (ii), every 2 h over 24 h in specified conditions. Bars show mean + SD. (C) Bar plots showing the percentage of neutrophil migration at $t = 12$ h (i) and the rate of neutrophil accumulation (ii) at $t = 2$ h as representative time points. Bars show mean ± SD with mean values written above the points. Each data point represents an NTI-chip and $n = 8$ chips per condition. At least four independent experiments were performed. ANOVA with Tukey multiple comparisons test was performed for comparisons between N0, N1, and N2 conditions at each time point. ns: $p > 0.05$, *: $p < 0.05$, **: $p < 0.01$, ***: $p < 0.001$. Asterisks in (B) represent the significance of differences between N1-like and N2-like neutrophils. Time points without asterisks mean no statistically significant differences.

N2-like neutrophils show greater migration toward PANC-1 cancer cells and higher motility after migration than N1-like neutrophils

In scenario 1, we examined the migratory behaviors of different neutrophil subtypes toward cancer cells. Side channel A was loaded with individual PANC-1 cancer cells embedded in collagen hydrogel to mimic the extracellular matrix of the tumor tissue. The central channel was loaded with N0, N1-like, or N2-like neutrophils embedded in collagen hydrogel. Side channel B was loaded with empty hydrogel without cancer cells, acting as a negative control. Using time-lapse imaging of the NTI-chip, we captured the temporal dynamics of neutrophil migration from the central channel into side channels A and B every 2 h over 24 h (Fig. 3A and S5A; Video S1). Neutrophil migration to cancer

was quantified as the percentage of neutrophils that migrated into side channel A, and neutrophil migration to empty gel as the percentage of neutrophils that migrated into side channel B. The percentage of migration into side channel A (cancer cells) was higher than that into side channel B (empty gel control) over the course of 24 h for all three neutrophil subtypes ($p < 0.01$) (Fig. S5), thus showing the ability of neutrophils to migrate toward PANC-1 cancer cells. Importantly, N2-like neutrophils showed a higher percentage of migration to cancer cells than N1-like neutrophils at all examined time points from $t = 2$ h to $t = 24$ h (3.41% vs. 0.19%, $p < 0.01$ at $t = 2$ h; 5.39% vs. 1.58%, $p < 0.05$ at $t = 12$ h; 5.54% vs. 2.56%, $p = 0.24$ at $t = 24$ h) (Fig. 3Bi and Ci). N2-like neutrophils showed a lower percentage of migration than N0 neutrophils (3.41% vs. 4.03%, $p = 0.72$ at $t = 2$ h; 5.39% vs. 7.19%, $p = 0.47$ at $t = 12$ h; 5.54% vs. 8.44%, $p = 0.28$ at $t =$
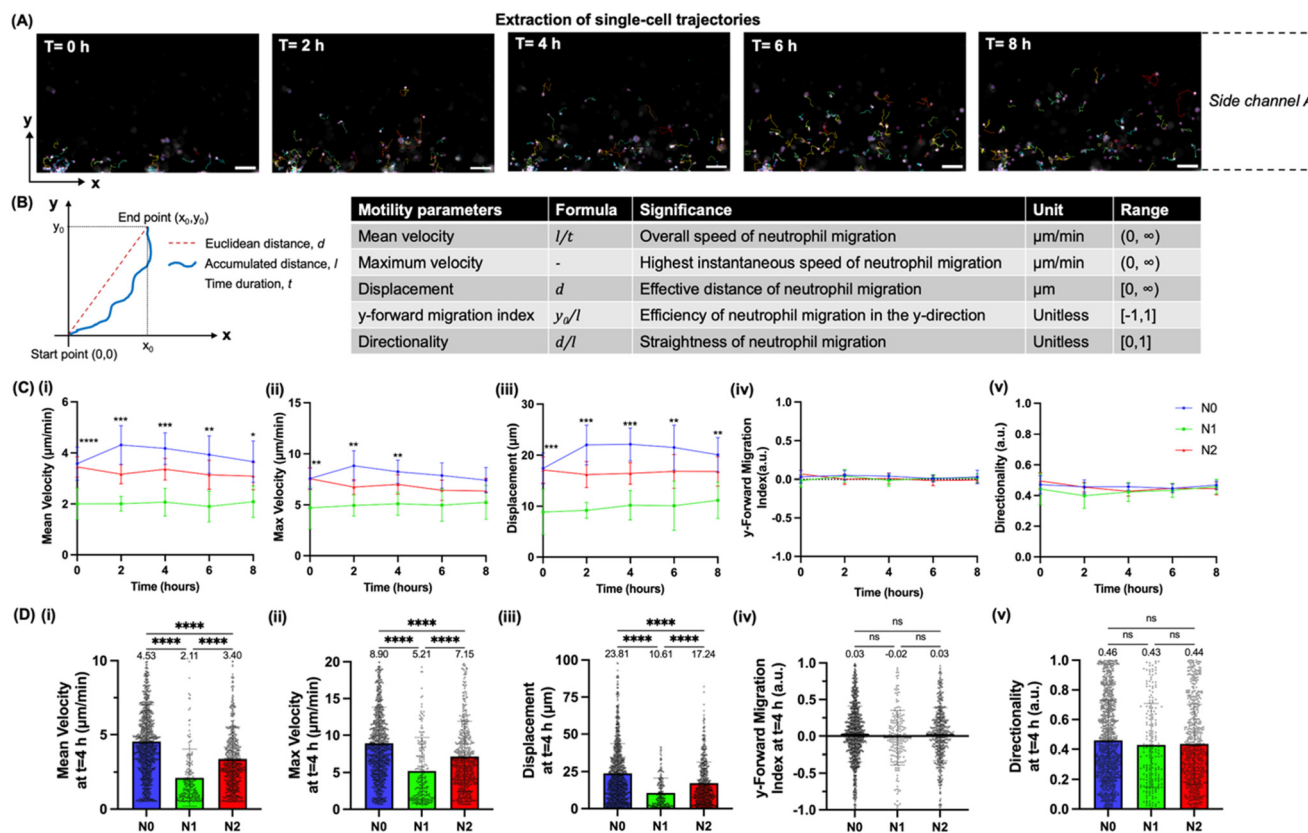

Fig. 4 In scenario 1, N2-like neutrophils show higher motility than N1-like neutrophils after migration toward PANC-1 cancer cells. (A) Representative 10× images showing the single-cell trajectories (color-coded) of neutrophils (white) after migration into side channel A housing cancer cells (not shown) at $t = 0$ h, 2 h, 4 h, 6 h, and 8 h of time-lapse imaging. Neutrophils were tracked over 20 min intervals every 2 h using TrackMate (ImageJ). Scale bar, 100 μm. (B) Definitions and significances of the following motility parameters of a single-cell trajectory: mean velocity, maximum velocity, displacement, y-forward migration index (y-FMI), and directionality. (C) Line graphs showing the mean velocity (i), maximum velocity (ii), displacement (iii), y-FMI (iv), and directionality (v) of motile neutrophils every 2 h over 8 h in N0, N1, and N2 conditions. Each data point represents the average value of all tracked neutrophils per NTI-chip and $n = 9$ chips per condition. Bars show mean ± SD. Ordinary one-way ANOVA was performed for comparisons between N0, N1, and N2 conditions at each time point. *: $p < 0.05$, **: $p < 0.01$, ***: $p < 0.001$, ****: $p < 0.0001$. Asterisks represent the significance of differences between N1-like and N2-like neutrophils. Time points without asterisks mean no statistically significant differences. (D) Bar plots showing the mean velocity (i), maximum velocity (ii), displacement (iii), y-FMI (iv), and directionality (v) of motile neutrophils with single-cell resolution at $t = 4$ h as a representative time point in specified conditions. Each data point represents a single neutrophil and $n = 202$–1042 neutrophils per condition. Bars show mean ± SD with mean values written above the points. At least four independent experiments were performed. ns: ≥0.05, ***: $p < 0.001$, ****: $p < 0.0001$, Kruskal–Wallis test.

24 h), although the differences were not statistically significant (Fig. 3Bi and Ci). N2-like neutrophils also showed a higher rate of accumulation inside side channel A (measured as the increase in the percentage of migration per hour) than N1-like neutrophils at $t = 2$ h (1.71 vs. 0.10% h^{-1}, $p < 0.01$) (Fig. 3Bii and Cii). These results suggest that pro-tumor (N2) neutrophils may be more capable of migrating to the tumor tissue than anti-tumor (N1) neutrophils.

We also captured the motility of different neutrophil subtypes after migration into side channel A every 2 h over the first 8 h of time-lapse imaging. We first extracted neutrophil trajectories at each time point ($t = 0$ h, 2 h, 4 h, 6 h, and 8 h) (Fig. 4A; Video S2) and then quantified the following motility parameters of each trajectory with single-neutrophil resolution: mean velocity, maximum velocity, displacement, y-forward migration index (y-FMI), and directionality (definitions illustrated in Fig. 4B). We presented the results using the average values of all tracked neutrophils per chip as population measures in Fig. 4C and S6 and using the values of each tracked neutrophil at $t = 4$ h as a representative time point in Fig. 4D. We found that N0 neutrophils showed an overall higher motility than N2-like neutrophils at all examined time points from $t = 0$ h to $t = 8$ h in terms of mean velocity (4.53 vs. 3.40 μm min^{-1} at $t = 4$ h), maximum velocity (8.90 vs. 7.15 μm min^{-1} at $t = 4$ h), and displacement (23.81 vs. 17.24 μm at $t = 4$ h) ($p < 0.0001$) (Fig. 4C and Di–iii and S6). Importantly, N2-like neutrophils showed an overall higher motility than N1-like neutrophils at all examined time points from $t = 0$ h to $t = 8$ h in terms of mean velocity (3.40 vs. 2.11 μm min^{-1} at $t = 4$ h), maximum velocity (7.15 vs. 5.21 μm min^{-1} at $t = 4$ h), and displacement (17.24 vs. 10.61 μm at $t = 4$ h) ($p < 0.0001$) (Fig. 4C and Di–iii and S6). Nonetheless, no statistically significant differences were found between N0, N1-like, and N2-like neutrophils in y-FMI (0.03 vs. −0.02 vs. 0.03 at $t = 4$ h) and directionality (0.46 vs. 0.43 vs. 0.44 at $t = 4$ h) (Fig. 4C and Div and v and S6). These results suggest that pro-tumor (N2) neutrophils may be more motile than anti-tumor (N1) neutrophils after migration into the tumor tissue. The lower motility of N1-like neutrophils could be due to their downregulation of chemokine receptor CXCR2 (CD182) compared to N0 and N2-like neutrophils (Fig. 2Biv and S2D) and thus a reduced responsiveness to cancer cell-secreted chemokines. The underlying reason for the higher motility of N0 neutrophils than N2-like neutrophils remains unclear and can be investigated by examining the gene expression differences between the two cell types via qPCR or RNA-sequencing in the future. The wide distribution in motility among individual neutrophils from each condition may suggest the existence of subpopulations within each subtype of neutrophils (N0, N1-like and N2-like neutrophils) that warrants further investigation.

N1-like neutrophils engage in longer contact with PANC-1 tumor spheroids than N2-like neutrophils

After studying the differences between N0, N1-like, and N2-like neutrophils in migration to cancer and post-migration motility in scenario 1, we sought to examine the neutrophil–cancer contact inside the tumor tissue. To achieve this purpose, we used PANC-1 tumor spheroids (3D cancer cell aggregates) in scenario 2, a format that more closely mimics the solid tumor tissue in vivo than individual cancer cells used in scenario 1. In scenario 2, N0, N1-like, or N2-like neutrophils, together with tumor spheroids, were embedded in collagen hydrogel which mimics the extracellular matrix of the tumor tissue and loaded into side channels A and B of the NTI-chip. Using time-lapse imaging of the NTI-chip, we captured the temporal dynamics of contact between different neutrophil subtypes and tumor spheroids over 6 h. For each tumor spheroid, we measured both the frequency and duration of contact with the surrounding neutrophils. Here, contact is defined as a situation in which the distance between the center of a tumor spheroid and the center of a neutrophil is less than the sum of the radius of the tumor spheroid and the diameter of the neutrophil[47,51,53] (Fig. 5A). The frequency of contact is the number of times that a given tumor spheroid formed contact with any neutrophil. The duration of contact is the length of time for which the contact between each neutrophil and the tumor spheroid lasted. We first found that both N1-like and N2-like neutrophils showed similar frequencies of contact with tumor spheroids (10.1 vs. 9.5, $p > 0.999$) and showed higher frequencies of contact with tumor spheroids than N0 neutrophils (10.1 vs. 4.5; 9.5 vs. 4.5, $p < 0.0001$) (Fig. 5B and Ci; Videos S3–S5). The rate of contact is defined as the frequency of contact divided by the total duration of imaging (6 h). Thus, the mean rates of contact for N0, N1-like, and N2-like neutrophils are 0.75 times per h, 1.68 times per h, and 1.58 times per h, respectively. Nonetheless, N1-like neutrophils showed a longer mean duration of contact per tumor spheroid than N2-like neutrophils (32.7 vs. 20.3 min, $p < 0.0001$) (Fig. 5B and Cii; Videos S2–S4). To further probe the contact with single-neutrophil resolution, we then analyzed the duration of contact per neutrophil instead of the mean values per spheroid. The distributions and quartiles of the durations of contact per neutrophil for N0, N1-like, and N2-like neutrophils are reported in Fig. S7. The frequency distributions of durations of contact per neutrophil showed an increase in the frequency of durations of contact longer than 30 min in N1-like neutrophils compared to N2-like and N0 neutrophils (Fig. 5D). Thus, we classified all contacts into two arbitrary categories: short contacts (≤30 min) and long contacts (>30 min).[51] While there was no significant difference in the duration of short contact between N0, N1-like, and N2-like neutrophils (14.2 vs. 13.9 vs. 13.6 min, $p = 0.174$), N1-like neutrophils showed a longer duration of long contact than N2-like and N0 neutrophils (80.8 vs. 62.4 min, $p = 0.026$; 80.8 vs. 59.7 min, $p = 0.006$) (Fig. 5E). Overall, these results showed that N1-like neutrophils engaged in longer contact with tumor spheroids than N2-like neutrophils, suggesting that anti-tumor neutrophils may form longer contact with cancer cells in the tumor tissue than pro-tumor neutrophils. The observed difference could be possibly due to the upregulation of intercellular adhesion molecule ICAM-1 (CD54) in N1-like neutrophils compared to N2-like neutrophils (Fig. 2Bii), leading to a stronger adhesion of N1-like neutrophils with tumor spheroids. The molecular mechanisms underlying the
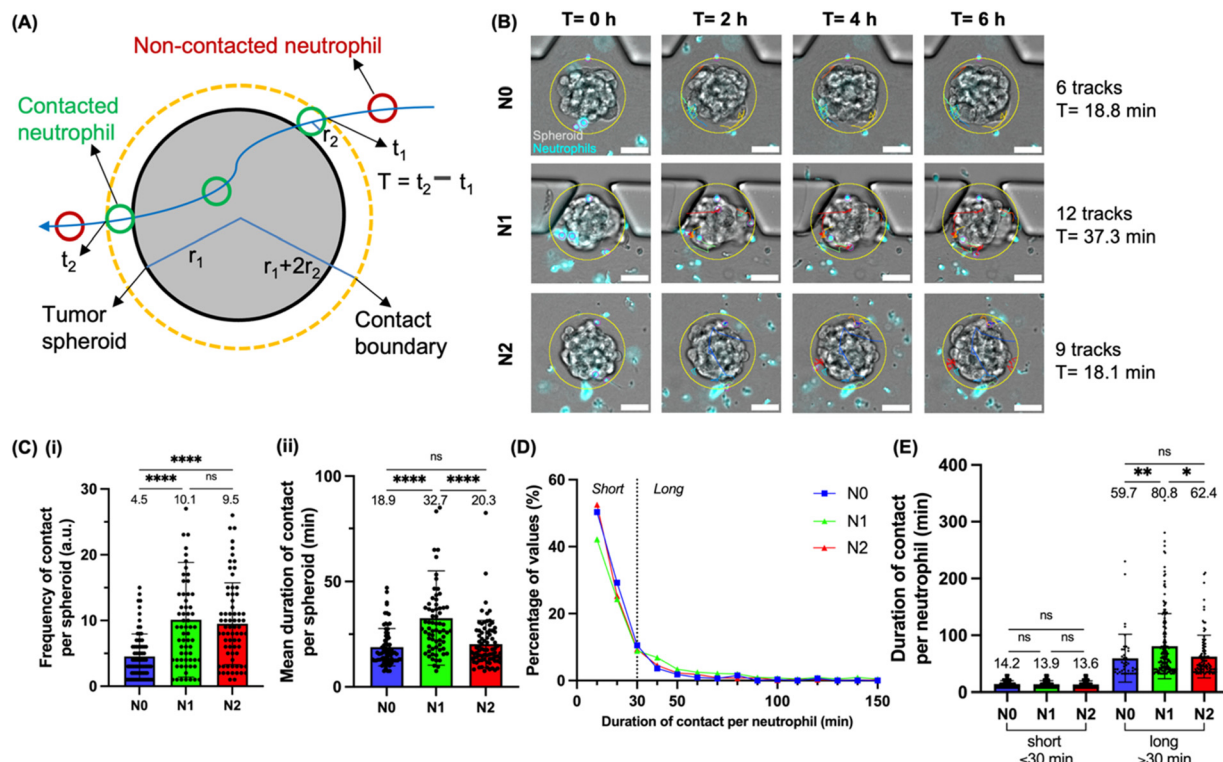
Fig. 5 In scenario 2, N1-like neutrophils engage in longer contact with PANC-1 tumor spheroids than N2-like neutrophils. (A) A schematic showing the definition of contact between a motile neutrophil (track shown in blue) and a given tumor spheroid. r_1 = radius of the tumor spheroid, r_2 = radius of a neutrophil. T = duration of contact. Black = boundary of the tumor spheroid, orange = boundary of the circular "contact" region with a radius of $r_1 + 2 \times r_2$, green = neutrophils in contact, red = neutrophils not in contact. Only contacts longer than 5 min were included to remove random collisions. (B) Representative 10× images showing N0, N1-like, and N2-like neutrophils (blue) interacting with tumor spheroids (brightfield) at t = 0 h, 2 h, 4 h, and 6 h of time-lapse imaging, overlaid with neutrophil tracks (color-coded) extracted by TrackMate. Any neutrophils that entered the circular ROI (yellow) around the spheroid were considered to be in contact with the spheroid. The number of neutrophil tracks (frequency) and the mean duration of contact for each image are shown on the right side. Scale bar, 50 μm. (C) Bar plots showing the frequency (i) and mean duration (ii) of contact with N0, N1-like, and N2-like neutrophils per tumor spheroid over 6 h. Each data point represents a spheroid and n = 68–79 spheroids per condition. Bars show mean ± SD with mean values written above the points. (D) Distributions of durations of contact per neutrophil in specified conditions. Only contacts shorter than 150 min are shown. (E) Contact between a neutrophil and a tumor spheroid was classified into two categories: short (≤30 min) and long (>30 min). A bar plot showing the duration of contact per neutrophil in specified conditions. Each data point represents a neutrophil and n = 332–708 neutrophils per condition. Bars show mean ± SD with mean values written above the points. At least three independent experiments were performed. ns: ≥0.05, *: $p < 0.05$, **: $p < 0.01$, ****: $p < 0.0001$, Kruskal–Wallis test.

differences in the tumor contact dynamics between different neutrophil subtypes warrant further investigation.

N1-like neutrophils show greater infiltration into PANC-1 tumor spheroids than N2-like neutrophils

After quantifying the contact of different neutrophil subtypes with tumor spheroids as a real-time behavior, we also assessed the infiltration of N0, N1-like, and N2-like neutrophils into tumor spheroids after 24 h incubation using end-point confocal imaging of the NTI-chip. Using 3D image analysis software Imaris, we quantified both the number of infiltrated neutrophils per tumor spheroid and the infiltration depth per neutrophil. Specifically, the shortest distance of a neutrophil to the 3D surface of a given tumor spheroid was measured, and neutrophils located outside the tumor spheroid would have positive values and those located inside the tumor spheroid would have negative values. Here, any neutrophil whose

shortest distance to the spheroid surface is lower than the radius of the neutrophil, including those with negative values, was considered as infiltrated (Fig. 6A). Infiltration depth was defined as the absolute value of the shortest distance of an infiltrated neutrophil to the surface of the tumor spheroid[78] (Fig. 6A). We found a higher number of N1-like neutrophils that infiltrated into tumor spheroids than N2-like and N0 neutrophils (4.7 vs. 2.9 cells per spheroid, $p < 0.001$; 4.7 vs. 2.8 cells per spheroid, $p < 0.0001$) (Fig. 6B and Ci). There was no significant difference in infiltration depth between N0, N1-like, and N2-like neutrophils (6.9 vs. 7.6 vs. 6.6 μm, $p = 0.315$), although N1-like neutrophils showed a slight increase than the other two subtypes (Fig. 6Cii). The frequency distributions of infiltration depths per neutrophil also showed an increase in deep infiltration (arbitrarily defined as >15 μm) in N1-like neutrophils compared to N2-like and N0 neutrophils (Fig. 6D). These results showed an overall greater infiltration of N1-like neutrophils into tumor spheroids than N2-like neutrophils,
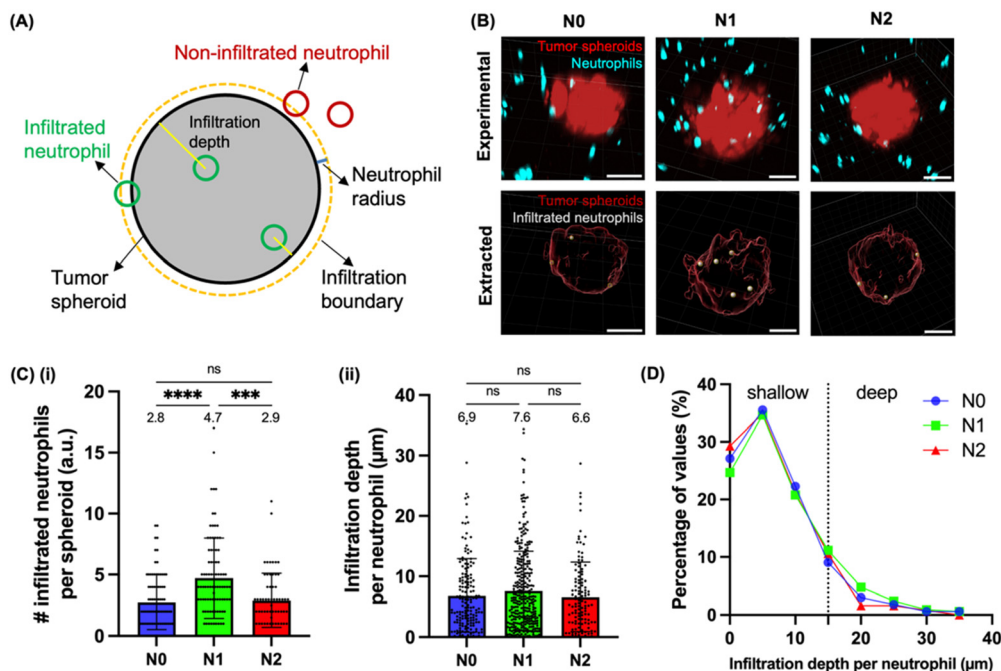
Fig. 6 In scenario 2, N1-like neutrophils show greater infiltration into PANC-1 tumor spheroids than N2-like neutrophils. (A) A schematic showing the definition of neutrophil infiltration in a given tumor spheroid. Black = boundary of the tumor spheroid, orange = infiltration boundary, green = infiltrated neutrophils, red = non-infiltrated neutrophils, yellow line = infiltration depth. Any neutrophil whose shortest distance to the spheroid surface is lower than the radius of the neutrophil, including those with negative values, was considered as infiltrated. Infiltration depth was defined as the absolute value of the shortest distance of an infiltrated neutrophil to the surface of the tumor spheroid. (B) 3D rendering of representative 10× confocal images showing the infiltration of N0, N1-like, and N2-like neutrophils (blue) in tumor spheroids (red) fixed at $t = 24$ h after neutrophils and tumor spheroids were loaded into the NTI-chip and the extraction of spheroid surfaces and infiltrated neutrophil spots by Imaris. Images were acquired as z-stacks with a 2 μm step size. Scale bar, 50 μm. (C) (i) A bar plot showing the number of infiltrated neutrophils per tumor spheroid in specified conditions. Each data point represents a spheroid and $n = 64$–91 spheroids per condition. (ii) A bar plot showing the infiltration depth per neutrophil in specified conditions. Each data point represents a neutrophil and $n = 123$–332 neutrophils per condition. Bars show mean ± SD with mean values written above the points. (D) Frequency distributions of infiltration depths per neutrophil in specified conditions. Infiltration depths less than 15 μm were arbitrarily defined as "shallow" and those greater than 15 μm as "deep". At least three independent experiments were performed. ns: ≥0.05, ***: $p < 0.001$, ****: $p < 0.0001$, Kruskal–Wallis test.

suggesting that anti-tumor neutrophils might have a greater ability to infiltrate into the solid tumor mass than pro-tumor neutrophils. The overall low number of tumor-infiltrated neutrophils of all three subtypes observed in this study could be partially attributed to the small size of the tumor spheroids (~100 μm in diameter shown in Fig. S1Cii) compared to those in previous studies of neutrophil–tumor infiltration (~250 μm and ~820 μm in diameter)[39,45,79] and thus a limited capacity of smaller spheroids to allow neutrophil infiltration. Larger tumor spheroids can be grown in a future study to allow for greater infiltration of different neutrophil subtypes. The infiltration state of neutrophils at other time points than $t = 24$ h were not examined here and can be measured as a real-time behavior using time-lapse confocal imaging in a future study.

N1-like neutrophils attenuate the invasion, proliferation, and epithelial–mesenchymal transition of PANC-1 tumor spheroids compared to N2-like neutrophils

After observing the distinct behaviors of N0, N1-like, and N2-like neutrophils in response to tumor spheroids, we went on to examine the reciprocal behaviors of tumor spheroids in

response to different neutrophil subtypes in the NTI-chip. Tumor invasion into the stroma is a critical step in metastasis *in vivo*,[80,81] as cancer cells in the primary tumor site must first invade into the surrounding extracellular matrix before entering the bloodstream and finally seeding at a secondary site in a distant organ to complete metastasis.[82] Therefore, we measured the invasion of tumor spheroids into the surrounding gel matrix as an early-stage behavior of metastasis under the influence of different neutrophil subtypes. We quantified spheroid invasion over 24 h in the NTI-chip by measuring the normalized invasion area, defined as the difference between the final projected area of the spheroid ($t = 24$ h) and the initial projected area ($t = 0$ h) divided by the initial projected area[39,45,83–85] (Fig. 7Ai). We found that N1-like neutrophils reduced tumor spheroid invasion compared to N2-like neutrophils and N0 neutrophils, as evidenced by a reduction of normalized invasion area from 0.51 (N2-like, $p < 0.0001$) or 0.45 (N0, $p < 0.001$) to 0.35 (N1-like) (Fig. 7Aii and iii).

In addition to invasion, we also examined proliferation and epithelial–mesenchymal transition (EMT) as two other hallmarks of tumor progression. We measured the expression of proliferation marker Ki-67[70] and EMT marker
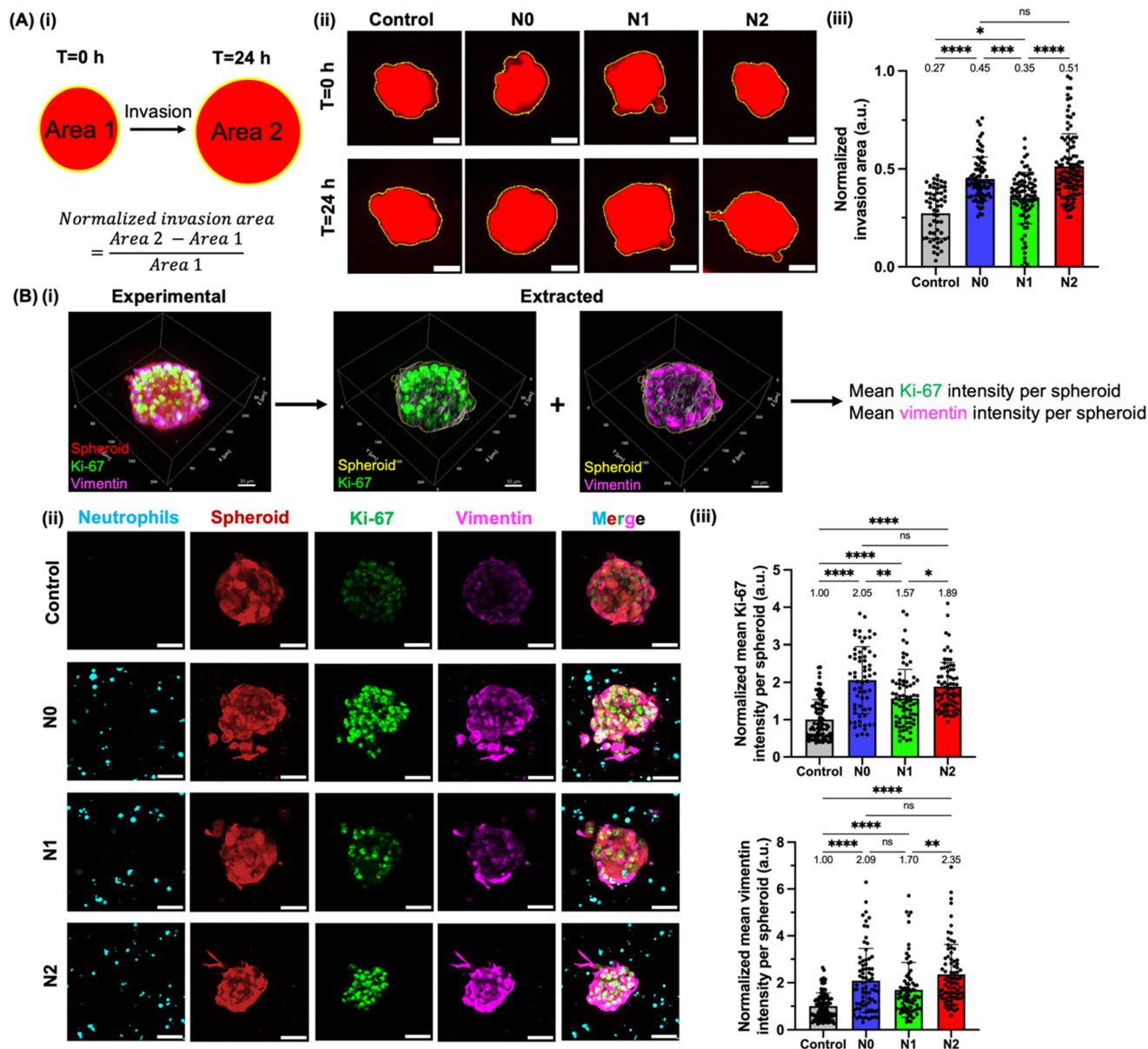
Fig. 7 In scenario 2, N1-like neutrophils attenuate the invasion, proliferation, and epithelial–mesenchymal transition (EMT) of PANC-1 tumor spheroids compared to N2-like neutrophils. (A) (i) Invasion of tumor spheroids into the surrounding collagen gel matrix was quantified by normalized invasion area, defined as the ratio of increase in the projected area of the invaded spheroid over 24 h to the initial projected area at $t =$ 0 h. (ii) Representative 10× epifluorescence images showing the invasion of tumor spheroids (red, boundaries circled in yellow) at $t =$ 0 h and 24 h after tumor spheroids were treated with culture medium (control), N0 neutrophils, N1-like neutrophils, or N2-like neutrophils in the NTI-chip. Scale bar, 50 μm. (iii) A bar plot showing the normalized invasion area of tumor spheroids in specified conditions. Each data point represents a spheroid and $n =$ 58–101 spheroids per condition. (B) (i) Representative 3D rendering of 20× confocal images showing tumor spheroids (red) immunostained for proliferation marker Ki-67 (green) and EMT marker vimentin (magenta) at $t =$ 24 h after tumor spheroids were loaded into the NTI-chip and the extraction of the spheroid volume (yellow) by Imaris. Images were acquired as z-stacks with a 2 μm step size. The mean Ki-67 intensity and vimentin intensity within the extracted spheroid volume were measured. Scale bar, 30 μm. (ii) Maximum intensity projections of representative 20× confocal images of neutrophils (blue) and tumor spheroids (red) immunostained for Ki-67 (green) and vimentin (magenta) at $t =$ 24 h in specified conditions. Scale bar, 50 μm. (iii) Bar plots showing the normalized mean Ki-67 intensity (upper panel) and vimentin intensity (lower panel) per tumor spheroid. Raw values were normalized by the mean of the control condition. $n =$ 74–113 spheroids per condition. Bars show mean ± SD with the mean values written above the points. At least three independent experiments were performed. ns: $p \geq 0.05$, *: $p <$ 0.05, **: $p < 0.01$, ****: $p < 0.0001$, Kruskal–Wallis test.

vimentin[67–69] by tumor spheroids using immunofluorescence and confocal imaging after 24 h incubation with different neutrophil subtypes in the NTI-chip. The levels of proliferation

and EMT of tumor spheroids were quantified as the mean Ki-67 intensity per spheroid and the mean vimentin intensity per spheroid, respectively (Fig. 7Bi). We found that N1-like

neutrophils reduced tumor proliferation compared to N2-like and N0 neutrophils, as evidenced by a reduction of mean Ki-67 intensity per spheroid from 1.89 (N2-like, $p = 0.038$) or 2.05 (N0, $p = 0.009$) to 1.57 (N1-like) (Fig. 7Bii). We also found that N1-like neutrophils reduced tumor EMT compared to N2-like neutrophils, as evidenced by a reduction of mean vimentin intensity per spheroid from 2.35 to 1.70 ($p = 0.001$) (Fig. 7Bii). N1-like neutrophils also led to a non-significantly lower level of tumor EMT than N0 neutrophils (1.70 *vs.* 2.09, $p = 0.478$) (Fig. 7Bii). Overall, these results show that N1-like neutrophils attenuated the progression of tumor spheroids compared to N2-like neutrophils in terms of invasion, proliferation, and EMT, which corroborates the anti-tumor nature of N1-like neutrophils and the pro-tumor nature of N2-like neutrophils in a 3D spheroid setting. Nonetheless, N1-like neutrophils still led to a higher level of invasion (0.35 *vs.* 0.27, $p = 0.028$), proliferation (1.57 *vs.* 1.00, $p < 0.0001$), and EMT (1.70 *vs.*

1.00, $p < 0.0001$) of tumor spheroids than the negative control condition without neutrophils (Fig. 7A and B). This result suggests the complexity of the secretome of N1-polarized neutrophils in this study and the need for alternative polarization methods to achieve a more profound anti-tumor therapeutic effect. Although showing a tumor-suppressive effect compared to N2-like and N0 neutrophils, N1-like neutrophils may still secrete certain soluble factors capable of promoting tumor progression. The secretomes of different neutrophil subtypes were not examined in this study and merit further investigation. Moreover, we found no significant difference between N0 and N2-like neutrophils in terms of invasion (0.45 *vs.* 0.51, $p = 0.255$), proliferation (2.05 *vs.* 1.89, $p > 0.999$), and EMT (2.09 *vs.* 2.35, $p = 0.363$) of tumor spheroids (Fig. 7A and B), suggesting that naïve N0 neutrophils may already resemble a pro-tumor phenotype even before N2 polarization.
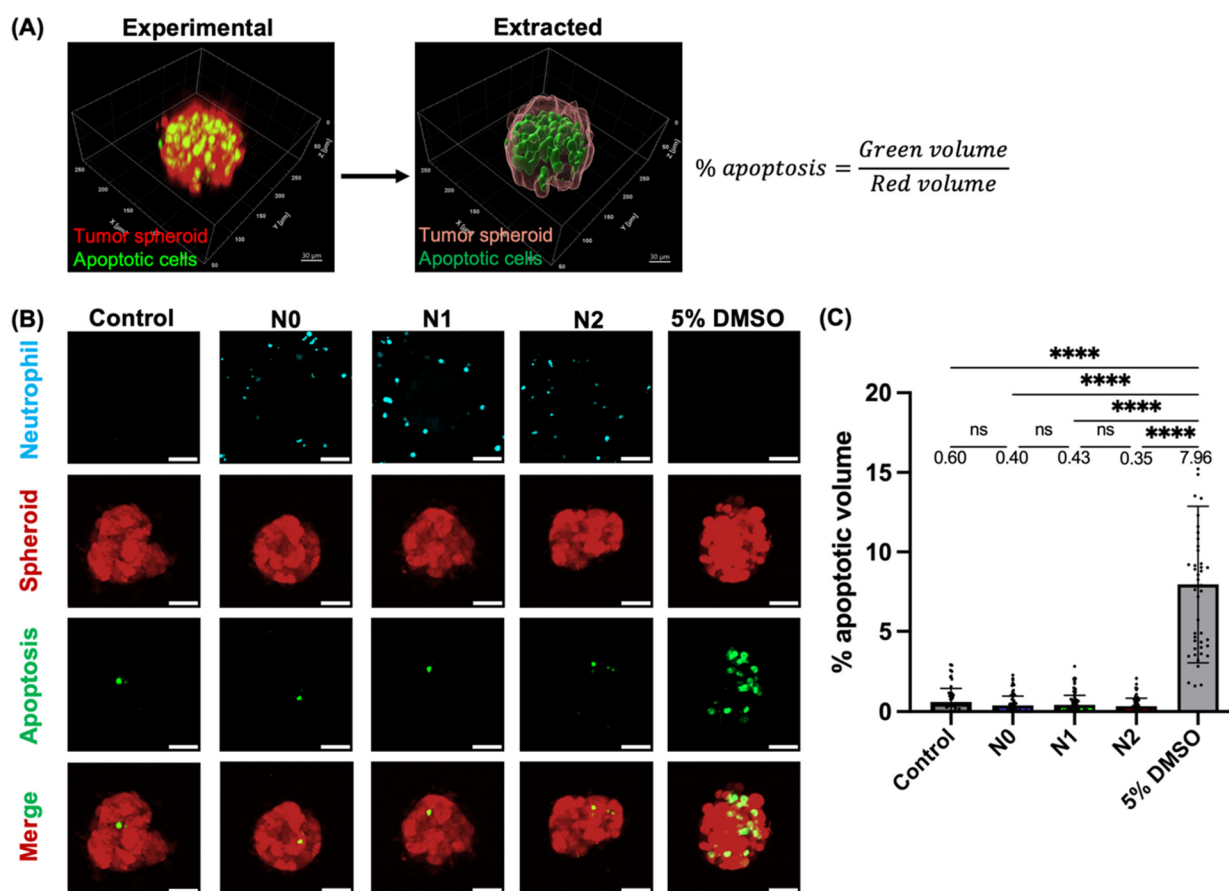

Fig. 8 In scenario 2, both N1-like and N2-like neutrophils induced limited apoptosis of PANC-1 tumor spheroids. (A) 3D rendering of representative 10× confocal images showing the apoptosis (caspase-3/7 green) of tumor spheroids (red) fixed at $t = 24$ h after tumor spheroids were loaded into the NTI-chip and the extraction of the apoptotic volume and the total spheroid volume by Imaris. Images were acquired as z-stacks with a 2 μm step size. Apoptotic signals co-localized with CellTracker Violet-stained neutrophils were excluded from the apoptotic volume to remove apoptotic neutrophils. Tumor apoptosis was quantified as the apoptotic volume divided by the total spheroid volume. Scale bar, 30 μm. (B) Maximum intensity projections of representative 10× confocal images showing the apoptosis (green) of tumor spheroids (red) treated with culture medium alone (control), N0 neutrophils, N1-like neutrophils, N2-like neutrophils, or 5% DMSO (positive control) for 24 h. Neutrophils (blue) were also shown. Scale bar, 50 μm. (C) A bar plot showing the percentage of apoptotic volume per tumor spheroid in specified conditions. Each data point represents a spheroid and $n = 45–89$ spheroids per condition. Bars show mean ± SD with mean values written above the points. At least three independent experiments were performed. ns: $p \geq 0.05$, ****: $p < 0.0001$, Kruskal–Wallis test.

Both N1-like and N2-like neutrophils demonstrate limited cytotoxicity against PANC-1 tumor spheroids

Lastly, we examined the apoptosis of tumor spheroids as a measure of neutrophil cytotoxicity. Using staining of apoptosis marker caspase-3/7[55,86] and end-point confocal imaging, we captured apoptosis after 24 h incubation with different neutrophil subtypes in the NTI-chip. We measured the total volume and the apoptotic volume of each tumor spheroid and quantified apoptosis as the percentage of apoptotic volume per spheroid (Fig. 8A). Interestingly, we found no significant difference in tumor spheroid apoptosis between N0, N1-like, and N2-like neutrophils (0.40% *vs.* 0.43% *vs.* 0.35%, $p > 0.999$) (Fig. 8B and C). There was also no significant difference

between the negative control condition without neutrophils (0.60%) and any of the three neutrophil subtypes ($p > 0.999$) (Fig. 8B and C). We then examined the effect of different neutrophil subtypes on the overall death of tumor spheroids using DRAQ7 staining as opposed to apoptosis alone, as neutrophils may exert cytotoxic effects through inducing other mechanisms of cell death than apoptosis. We found no significant difference in the overall death of tumor spheroids between N0, N1-like, and N2-like neutrophils (1.59% *vs.* 2.44% *vs.* 1.86%, $p > 0.999$), although there was a moderate increase in tumor death in the N1-like neutrophil condition compared to the negative control condition without neutrophils (2.44% *vs.* 1.10%, $p = 0.046$) (Fig. S8). Overall, these results showed a limited cytotoxicity of N1-like neutrophils against tumor
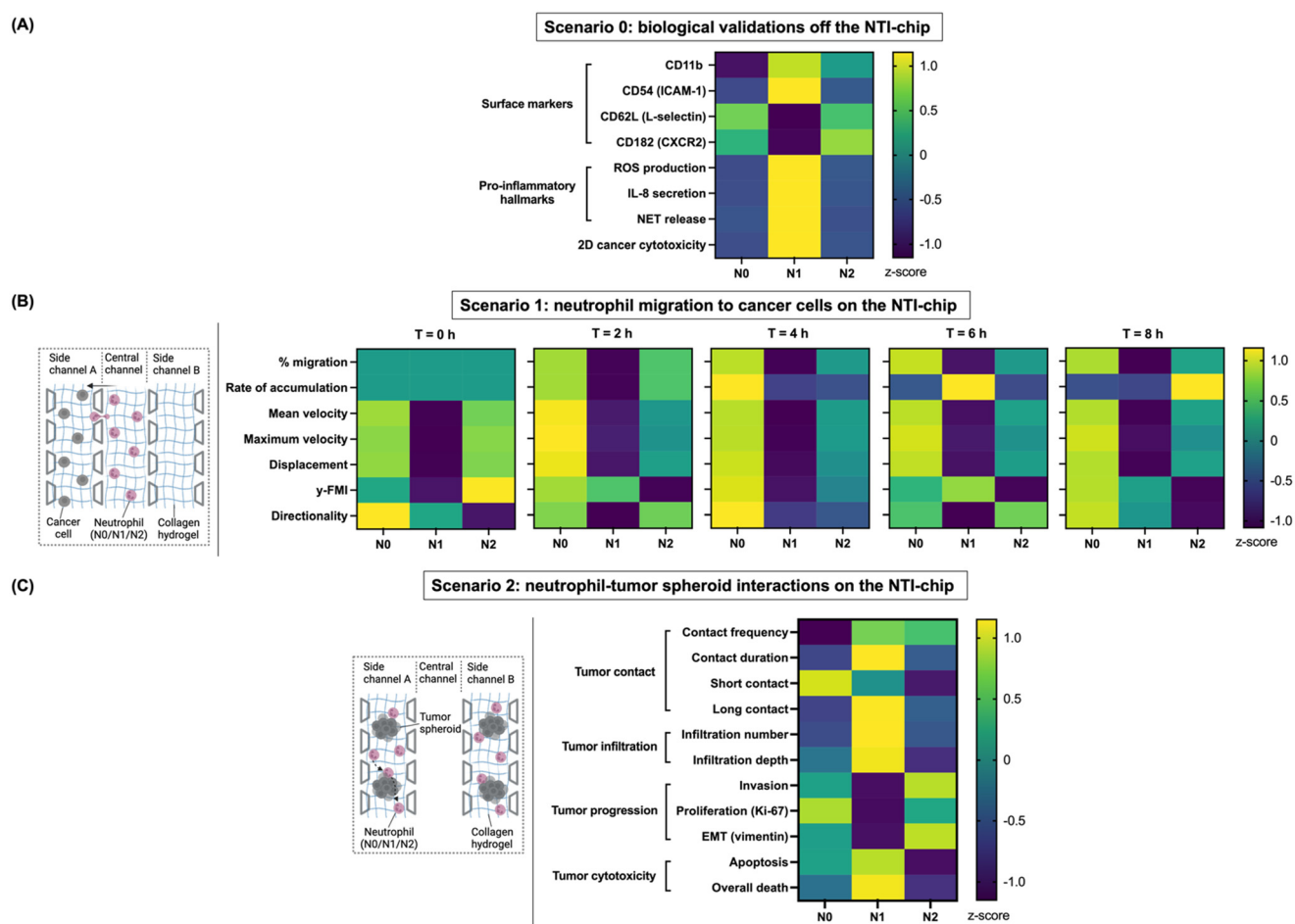

Fig. 9 Heatmaps summarizing the distinct behavioromes of N0, N1-like, and N2-like human neutrophils quantified in three scenarios. (A) In scenario 0 (off the NTI-chip), surface marker expressions, pro-inflammatory hallmarks, and 2D cancer cytotoxicity of neutrophils were validated on well plates. (B) In scenario 1 on the NTI-chip, we measured real-time behaviors of neutrophils at multiple time points including the percentage of migration to cancer cells, the rate of accumulation, and the post-migration motility in terms of mean velocity, maximum velocity, displacement, *y*-forward migration index, and directionality. (C) In scenario 2 on the NTI-chip, we measured neutrophil–tumor spheroid contact and tumor spheroid invasion as real-time behaviors, and neutrophil infiltration into tumor spheroids, proliferation and EMT of tumor spheroids, and neutrophil cytotoxicity against tumor spheroids as end-point behaviors. Each row of the heatmap represents a quantified behavior, and each column represents a condition (N0, N1, or N2). Z-Score normalization was used to transform the raw data so that each value represents the number of standard deviations away from the mean. Negative values are below the mean, while positive values are above the mean. The lower the value, the darker the color; the higher the value, the brighter the color. The neutrophil behaviorome quantified in this study adds a valuable dimension to the existing multi-omics approach in cancer immunology research.

spheroids. This could be partially explained by the greater difficulty of cancer killing in a 3D spheroid format than in a 2D monolayer format,[71,87] as cytotoxicity of N1-like neutrophils was observed in 2D monolayer co-cultures in Fig. 2F. A recent study of murine pancreatic cancer by Ng *et al.* shows that neutrophils of different initial states entering the tumor tissue all undergo deterministic reprogramming and converge into the same pro-tumor state.[88] Thus, it is also possible that anti-tumor N1-like neutrophils became corrupted by tumor spheroids over 24 h and eventually turned into a pro-tumor N2-like phenotype, thus diminishing their cytotoxic power. The potential phenotypic and transcriptional changes of N1-like neutrophils under the influence of tumor spheroids over the course of time were not examined in this study and warrants further investigation.

The NTI-chip enables the quantification of distinct behavioromes of N1-like and N2-like neutrophil subtypes

In this study, the NTI-chip enabled both real-time and end-point measurements of neutrophil–cancer interactions which formed a comprehensive "behaviorome" of N0, N1-like, and N2-like neutrophil subtypes, as summarized in heatmaps in Fig. 9. Specifically, we first performed an array of biological validations of the three neutrophil subtypes including surface marker expressions, pro-inflammatory hallmarks, and 2D cancer cytotoxicity on well plates, *i.e.*, off the NTI-chip (denoted as "scenario 0") (Fig. 9A). We then used the NTI-chip to quantify an array of real-time behaviors including neutrophil migration to cancer cells, rate of accumulation, and motility (mean velocity, maximum velocity, displacement, *y*-FMI, and directionality) in scenario 1, and kinetics of neutrophil–tumor spheroid contact (frequency and duration) and tumor spheroid invasion in the collagen gel matrix in scenario 2 (Fig. 9B and C). The detailed quantitative temporal information with single-neutrophil resolution enabled by live imaging of the NTI-chip would be difficult to attain using *in vivo* models and standard molecular biology assays.[36,73] We also quantified an array of end-point behaviors including neutrophil infiltration in tumor spheroids (abundance and depth), proliferation (Ki-67 expression) and epithelial–mesenchymal transition (vimentin expression) of tumor spheroids, and neutrophil cytotoxicity against tumor spheroids (apoptosis and overall death) in scenario 2 (Fig. 9C). The neutrophil behaviorome measured in this study adds a valuable dimension to the existing multi-omics paradigm that dominates the landscape of cancer immunology research.[36,87]

Discussion

In this work, we combined microfluidic technology with 3D cell culture and tissue engineering to construct a microphysiological system "NTI-chip" where we could examine human neutrophil–cancer interactions in a physiologically relevant microenvironment with single-cell resolution both in real time and at endpoints. The five-channel design of the NTI-chip, compared to three-channel designs,[89–92] enables the real-time monitoring of immune cell migration to cancer cells and end-

point immunofluorescence of markers in the same device. The increased width and height of the side channels compared to previously published dimensions[64,66] facilitate the loading of sizeable tumor spheroids into the channels. The NTI-chip also incorporated multiple biological components including 3D cancer cells and tumor spheroids, extracellular matrix-mimicking collagen hydrogel, and three subtypes of neutrophils (anti-tumor "N1", pro-tumor "N2", and neutral "N0"). This combination of microfluidics, tissue engineering, and immuno-oncology featured in our system presents a novel addition to the cause of using lab-on-a-chip technologies to tackle biomedical challenges. The NTI-chip also possesses several advantages for studying neutrophil–cancer interactions over traditional cell culture systems such as well plates. Firstly, the microposts in the NTI-chip enable different spatial arrangements of different cell types, *i.e.*, being positioned in two separate channels (scenario 1) or together in the same channel (scenario 2). In scenario 1, the NTI-chip allows for the spatial separation between neutrophils and cancer cells and real-time visualization of neutrophil migration from one channel to another (Fig. S9). The compartmentalization feature is absent in Petri dishes and well plates, while the real-time visualization feature is absent in transwell chambers.[34,35,37] Secondly, in contrast to the tall thickness of the hydrogel and thus uneven distances of different tumor spheroids to the objective lens of the microscope in well plates, the NTI-chip in scenario 2 ensures an almost even distance of different tumor spheroids to the objective lens due to the small height of its microfluidic channels relative to the diameter of the spheroid, which makes imaging faster and easier (Fig. S9). Thirdly, compared to large volumes in well plates, the small volume of microfluidic channels in the NTI-chip would also lead to faster diffusion and higher concentrations of biochemical signals secreted by cells and thus stronger neutrophil–cancer interactions and elevated neutrophil behaviors to be measured in our research[93–96] (Fig. S9).

In this study, we leveraged microfluidics to pioneer a quantitative "behaviorome" approach for studying different subtypes of neutrophils in pancreatic cancer, a recalcitrant solid tumor being the fourth leading cause of cancer-related deaths in the USA with a 5 year survival rate of only 9%.[7,97] For the first time, this study reveals that anti-tumor (N1-like) and pro-tumor (N2-like) human neutrophils indeed behave and interact with cancer differently in terms of migration, motility, contact, infiltration, and the effects on tumor progression. Our findings suggest that although anti-tumor neutrophils may be less capable of migrating to the tumor tissue and less motile than pro-tumor neutrophils, they could form longer contact with cancer cells in the tumor tissue and infiltrate better into the solid tumor mass than pro-tumor neutrophils. Such nuanced insight into the behavioral differences between neutrophil subtypes can inform the design and optimization of novel cancer immunotherapies in the future that aim to modulate specific neutrophil behaviors such as migration to tumor, contact with tumor, and infiltration into tumor. We also found a tumor-suppressive

effect of N1-like neutrophils in terms of invasion, proliferation, and EMT of tumor spheroids, but their tumor-killing ability was limited against tumor spheroids. These findings point to the need for more effective polarization or modification strategies to confer a stronger anti-tumor phenotype on neutrophils. Recent studies in mouse models have attempted to unleash and boost the anti-tumor activity of neutrophils to kill cancer cells in different ways.[98–101] Notably, Linde et al. developed an antibody cocktail therapy consisting of tumor necrosis factor (TNF), anti-CD40 monoclonal antibody, and a tumor-binding antibody to activate neutrophils.[98] Chang et al. genetically engineered chimeric antigen receptor (CAR)-neutrophils from human pluripotent stem cells for glioblastoma treatment.[99] We can utilize the NTI-chip to test and quantify the effects of these novel therapies on human neutrophil behaviors such as cytotoxicity against tumor spheroids in future studies.

The layout of the NTI-chip provides opportunities for recapitulating more physiologically complex scenarios to answer more intricate biological questions in the future. For example, we can study the preference of neutrophils in response to two competitive signals. Specifically, we can load neutrophils into the central channel and two different types of tumor-related signals in two side channels to examine the preferential migration of neutrophils towards either side.[50,73] We can also build an endothelium in the central channel to mimic the blood vessel wall[102–108] and measure the extravasation of N1-like and N2-like neutrophils from the central channel into the tumor spheroid-loaded side channel, which will contribute extravasation as another important behavior to the neutrophil behaviorome. Moreover, further studies are needed to better understand the molecular machinery that drives the distinct behavioromes between N1-like and N2-like neutrophils observed in this study; other-omes such as transcriptomes and proteomes can be examined to build a more comprehensive multi-omics profile for anti-tumor and pro-tumor human neutrophils in cancer. Furthermore, the simplistic N1/N2 terminology does not capture the entire spectrum of neutrophil diversity and plasticity in cancer.[20,109] Recent single-cell RNA sequencing studies in mice and human patients have revealed multiple distinct transcriptional states and clusters of neutrophils in tumors which go beyond the traditional N1/N2 binary concept.[88,100,101] Hence, a more nuanced and refined approach dealing with neutrophil subtypes can be adopted in future studies. Lastly, we only used immortalized human cell lines in this work, which limits its clinical relevance. Since only the neutrophil-like cell line HL-60 and the pancreatic cancer cell line PANC-1 were used, the conclusions in this study may not apply to primary human neutrophils and cancer cells or to other cancer cell lines. The NTI-chip will enable future research using sparse clinical samples of only a few microliters and a few thousand cells,[51] allowing for the measurement of interactions between patient-derived tumor cells and autologous neutrophils in the presence of drug candidates. This can open up avenues for personalized medicine and facilitate the translation of novel immunotherapies into cancer patients.[58,110] The US Food and Drug Administration (FDA) approved the first clinical trial based solely on organ-on-a-chip models in July 2022 and President Biden signed into law the FDA Modernization Act 2.0 adding "organ chips and microphysiological systems" to the list of nonclinical tests in December 2022.[111,112] Hence, it is now possible for complex in vitro models like the NTI-chip to serve as a crucial complementary tool to animal models for both cellular mechanism studies and preclinical testing of novel neutrophil-based cancer immunotherapies.[113]

Conclusions

In summary, we developed a human cell-based microphysiological system to quantitatively characterize the behavioral differences between anti-tumor N1-like and pro-tumor N2-like neutrophil subtypes in an engineered solid tumor microenvironment. We performed both real-time and end-point measurements of neutrophil–cancer interactions to form a comprehensive behaviorome consisting of neutrophil migration, motility, neutrophil-tumor spheroid contact, neutrophil–tumor spheroid infiltration, and invasion, proliferation, EMT, and apoptosis of tumor spheroids. We found that N2-like neutrophils showed greater migration to cancer cells and higher motility after migration than N1-like neutrophils. N1-like neutrophils engaged in longer contact with tumor spheroids and infiltrated greater into tumor spheroids than N2-like neutrophils. N1-like neutrophils also attenuated the progression of tumor spheroids in terms of invasion, proliferation, and EMT compared to N2-like neutrophils, although the tumor cytotoxicity of N1-like neutrophils was limited. The behaviorome measured in this study adds a valuable dimension to the existing multi-omics approach in cancer immunology research. The insight into the distinct behavioromes between anti-tumor and pro-tumor neutrophils can guide the development of novel cancer immunotherapies targeting specific neutrophil behaviors. In the future, the microphysiological system can be used to study the extravasation of different neutrophil subtypes into the tumor tissue and test novel therapeutic candidates using patient-derived tumor cells and autologous neutrophils for personalized medicine, thus holding strong potential to facilitate the clinical translation of therapeutics and improve human health.

Materials and methods

Cell culture

The human promyelocytic leukemia cell line HL-60 (American Type Culture Collection ATCC, CCL-240) was cultured in Iscove's modified Dulbecco's medium (IMDM, ATCC) supplemented with 20% fetal bovine serum (FBS, ATCC) and 1% penicillin–streptomycin (ATCC), denoted as complete IMDM. The red fluorescent protein (RFP)-transfected human pancreatic cancer cell line RFP-PANC-1 (FenicsBIO, CL-1191) was cultured in Dulbecco's modified Eagle's medium (DMEM, ATCC) supplemented with 10% FBS and 1% penicillin–streptomycin, denoted as complete DMEM. For passaging, RFP-PANC-1 cells

(abbreviated as PANC-1 cells) were detached using TrypLE™ Express Enzyme (Gibco) for 2 min at 37 °C with 5% CO_2. All cell cultures were maintained at 37 °C with 5% CO_2.

Differentiation and polarization of neutrophil-like HL-60 cells

HL-60 cells from passages 2 to 17 were seeded at a density of 2×10^5 cells per mL in T-25 culture flasks (10 mL per flask) and differentiated with 1.5% dimethyl sulfoxide (DMSO, ATCC) for 5 days into a neutrophil-like state (denoted as dHL-60 neutrophils).[73–75] dHL-60 neutrophils were then polarized for 24 h with 100 ng mL^{-1} lipopolysaccharide (LPS, Sigma Aldrich, L2630), 50 ng mL^{-1} interferon-γ (IFN-γ, R&D Systems, 285-IF-100/CF), and 50 ng mL^{-1} interferon-β (IFN-β, R&D Systems, 8499-IF-010/CF) to induce an N1-like (anti-tumor) phenotype[19] and with 100 ng mL^{-1} transforming growth factor-β (TGF-β, Sigma Aldrich, T7039) to induce an N2-like (pro-tumor) phenotype[24,25] as previously described. As a control for polarization, dHL-60 neutrophils were treated with the same volume of phosphate-buffered saline (PBS, Gibco) as a vehicle control for 24 h and denoted as N0 neutrophils. Both differentiation and polarization were performed at 37 °C with 5% CO_2. The mean and standard deviation among different experiments repeated for validating surface marker expressions by N1-like and N2-like neutrophils are listed in Table S1. The generation of N1-like and N2-like neutrophils using the HL-60 cell line was robust and reproducible, as shown by the standard deviation being less than 8% of the mean value for all markers (Table S1).

3D tumor spheroid culture

PANC-1 cells were harvested from passages 3 to 44 for 3D tumor spheroid culture. 3D tumor spheroids were generated using the Elplasia™ round-bottom ultra-low attachment (ULA) six-well plate (Corning, 4440) according to the manufacturer's protocol. Briefly, each well on the plate was prewetted with 1.5 mL of complete DMEM supplemented with 1% Matrigel (Corning, 354277) and centrifuged to remove air bubbles from the microcavities. Each well was then seeded with 1.5 mL of ~86 550 PANC-1 cells (~30 cells per microcavity, 2885 microcavities per well) in complete DMEM supplemented with 1% Matrigel to induce spheroid formation.[114,115] The plate was then incubated at 37 °C with 5% CO_2 for 48 h to form one spheroid in each microcavity with an average diameter of 96.7 ± 17.6 μm (Fig. S1Cii).

Design and fabrication of the NTI-chip

The NTI-chip comprises a central channel for loading culture medium (9 mm long, 400 μm wide), two side channels A and B for loading PANC-1 tumor spheroids and dHL-60 neutrophils (N0, N1-like, or N2-like) embedded in hydrogel mimicking the extracellular matrix of the tumor tissue (9 mm long, 700 μm wide), and two medium channels, each having two medium reservoirs for loading culture medium (6.7 mm long, 1 mm wide) (Fig. 1A). The two side channels served as technical duplicates of each other. The five parallel channels

are approximately 148 μm in height and interconnected by four arrays of 16 trapezoidal posts (base lengths: 200 μm and 84 μm, height: 100 μm, distance between posts: 50 μm) that enable the confinement of hydrogel through a balance between surface tension and capillary forces.[51]

The master mold was fabricated using standard photolithography techniques in the cleanroom. Briefly, the design of the NTI-chip was drawn in AutoCAD (Autodesk) and printed onto a chrome-on-glass dark-field photomask. A silicon wafer (University Wafer) was spin-coated with negative photoresist SU-8 50 (Kayaku Advanced Materials) at 1000 rpm for 30 s and soft-baked at 65 °C for 10 min and 95 °C for 2.5 h. The silicon wafer was exposed to ultraviolet (UV) light through the photomask at 450 mJ cm^{-2}. The exposed wafer was then baked at 65 °C for 1 min and 95 °C for 10 min and developed with SU-8 developer for 16 min. Lastly, the height of the features on the wafer was measured by a profilometer.

NTI-chips were fabricated using standard soft lithography techniques. Briefly, polydimethylsiloxane (PDMS) and the curing agent (Sylgard 184, Dow Corning) were mixed thoroughly at a 10 : 1 ratio, degassed in a desiccator for 1 h, poured over the master mold, and cured in an oven at 65 °C overnight. Solidified PDMS was then peeled from the master mold and individual chips were cut out. The inlets and outlets of the two medium channels were punched using a 4 mm biopsy puncher (Ted Pella Inc.) to create medium reservoirs and those of the two side channels and the central channel using a 1 mm biopsy puncher. Following air plasma treatment (Harrick Plasma) at high radio frequency (RF) power for 2 min, six chips were bonded to a glass-bottom six-well plate (Cellvis, P061.5HN) and placed on a hotplate at 80 °C overnight to strengthen bonding and restore hydrophobicity.[116] The NTI-chips were sterilized under UV light in a biosafety cabinet for 30 min before use.

Neutrophil migration toward cancer cells in the NTI-chip

1 mL of cold sterile water was dispensed around each NTI-chip on the glass-bottom six-well plate to maintain humidity and minimize evaporation. To prepare 200 μL of a 1.2 mg mL^{-1} collagen gel solution with a pH of 7.4, 80 μL of 3 mg mL^{-1} rat-tail type I collagen gel (Corning, 354236) was diluted in a mixture of 20 μL of 10× phosphate-buffered saline (PBS, Gibco), 96 μL of sterile deionized water, and 4 μL of 0.5 N NaOH (Fisher Chemical) on ice. The final pH of the gel solution was confirmed to be ~7.4 using a pH indicator paper. ~18 000 PANC-1 cancer cells (3×10^6 cells per mL) in 6 μL of collagen gel solution was loaded into side channel A of the NTI-chip on ice to mimic the tumor tissue. 6 μL of collagen gel solution alone was loaded into side channel B on ice to act as a negative control. The NTI-chips were incubated at 37 °C with 5% CO_2 for 30 min to polymerize the gel. The two medium channels were then filled with 100 μL of complete IMDM respectively to keep the cells alive and hydrated. The NTI-chips were then incubated at 37 °C with 5% CO_2 for 24 h to allow cancer cells to secrete neutrophil-

attracting chemokines before loading neutrophils into the central channel. The central channel was left empty (filled with air) during the 24 h incubation to prevent cancer-secreted chemokines from diffusing into empty gel in side channel B, which would undermine the chemical gradient needed for neutrophil migration. N0, N1-like, and N2-like dHL-60 neutrophils were collected after 24 h polarization, stained with Vybrant™ DiD dye (1 : 1000, Invitrogen, V22887) at 37 °C for 20 min, and washed once with complete IMDM to terminate staining. After 24 h incubation of the NTI-chips, ~30 000 dHL-60 neutrophils (5×10^6 cells per mL) in 6 μL of collagen gel solution was loaded into the central channel on ice. After 30 min gel polymerization, the NTI-chips were immediately time-lapse imaged to capture neutrophil migration and motility.

Neutrophil–tumor spheroid interactions in the NTI-chip

N0, N1-like, and N2-like dHL-60 neutrophils were collected after 24 h polarization, stained with 10 μM CellTracker Violet BMQC dye (Invitrogen, C2110) at 37 °C for 30 min,[64,92] and washed once with complete IMDM to terminate staining. PANC-1 tumor spheroids were collected from the ULA six-well plate after 48 h of 3D culture. All pipette tips used to transfer tumor spheroids were pre-coated with 2% bovine serum albumin (BSA, Sigma-Aldrich) to reduce spheroid loss. 1 mL of cold sterile water was dispensed around each NTI-chip on the glass-bottom six-well plate to maintain humidity and minimize evaporation. To prepare 200 μL of a 2.5 mg mL^{-1} collagen gel solution with a pH of 7.4, 166.7 μL of 3 mg mL^{-1} rat-tail type I collagen gel was diluted in a mixture of 20 μL of 10× PBS, 4.3 μL of sterile deionized water, and 9 μL of 0.5 N NaOH on ice.[92,116] The final pH of the gel solution was confirmed to be ~7.4 using a pH indicator paper. A mixture of ~9 tumor spheroids and ~30 000 dHL-60 neutrophils (5×10^6 cells per mL) in 6 μL of collagen gel solution was loaded into each of the two side channels of the NTI-chip on ice to mimic the tumor tissue. dHL-60 neutrophils alone without tumor spheroids in gel was loaded to assess baseline motility of neutrophils. Tumor spheroids alone without dHL-60 neutrophils in gel were loaded to assess baseline apoptosis of tumor spheroids. The NTI-chips were incubated at 37 °C with 5% CO$_2$ for 30 min to polymerize the gel. The two medium channels and the central channel were then filled with 100 μL and 7 μL of complete IMDM respectively to keep the cells alive and hydrated. To create a positive control condition for tumor spheroid death and apoptosis, complete IMDM containing 5% DMSO, a small molecule known to kill cancer cells,[92,117] was used to fill the NTI-chips. To capture tumor spheroid apoptosis at the endpoint using confocal imaging, the culture medium was pre-treated with 2 μM CellEvent™ Caspase-3/7 Green (Invitrogen, C10423) before loading into the NTI-chips.[51,55,86] To capture the overall death of tumor spheroids at the endpoint using confocal imaging, the culture medium was pre-treated with 3 μM DRAQ7 (BioLegend, 424001) before loading into the NTI-chips.[92,118]

Time-lapse imaging and analysis

Time-lapse live imaging of six NTI-chips was performed concurrently on a fully automated Nikon ECLIPSE Ti2-E microscope using a Plan Apo 10× objective (NA = 0.45) at 37 °C with 5% CO$_2$ for 24 h. In scenario 1, images were acquired using NIS-elements (Nikon Inc.) software and recorded using brightfield, Cy5 (neutrophils), and TRITC (cancer cells) channels at 2 h intervals for 24 h to capture neutrophil migration from the central channel into side channel A housing cancer cells. Images were also acquired every 2 min for 20 min at 2 h intervals for the first 8 h to enable cell tracking and measurement of neutrophil motility after migration into side channel A.[102] In scenario 2, images were acquired using NIS-elements software and recorded using brightfield, DAPI (neutrophils), and mCherry (tumor spheroids) channels at 2.5 min intervals for the first 6 h for cell tracking and at 1 h intervals for the remaining 18 h to minimize photobleaching over time. The goal was to capture the contact dynamics between neutrophils and tumor spheroids and the invasion of tumor spheroids in the gel matrix.

To quantify neutrophil migration in scenario 1, the number of cells in side channel A every 2 h was counted using the TrackMate plugin in ImageJ (National Institutes of Health) and divided by the number of cells initially in the central channel at $t = 0$ h for normalization.[102] To quantify neutrophil motility in side channel A in scenario 1, automatic cell tracking was performed on Cy5 images for every 20 min duration using TrackMate.[53,119] The following parameters of cell motility were exported from TrackMate for statistical analysis: mean velocity, maximum velocity, displacement (Euclidean distance), and directionality (linearity of forward progression) (Fig. 4B). The y-forward migration index (y-FMI) of neutrophils was quantified using the Chemotaxis and Migration Tool plugin (Ibidi) in ImageJ by importing the raw positional data exported from TrackMate (Fig. 4B).[120] Only tracks whose mean velocity was higher than 0.50 μm min^{-1} were used for analysis to exclude non-motile cells.

To quantify neutrophil–tumor spheroid contact in scenario 2, a circular region of interest (ROI) was defined around a certain tumor spheroid using brightfield images in ImageJ.[47,50,51,53] The diameter of the ROI equals the sum of the measured diameter of the tumor spheroid at $t = 0$ h and twice the diameter of an average neutrophil (13 μm) (Fig. 4A). The center of the ROI was manually placed at the approximate center of the tumor spheroid at $t = 0$ h. Any neutrophils that entered this ROI were considered to be in contact with the tumor spheroid. Automatic tracking of neutrophils within the circular ROI was performed on DAPI images from 0 to 6 h using TrackMate. The number of detected tracks is the frequency or the number of times that a neutrophil formed contact with the tumor spheroid. The duration of each track is the duration of contact between each neutrophil and the tumor spheroid. Only durations longer than 5 min were counted to exclude random collisions between neutrophils and tumor spheroids.[55] The mean

duration of contact per tumor spheroid was calculated by averaging durations of all tracks per ROI. The approach of modeling tumor spheroids and neutrophils as round objects in this study is an approximation, and thus a more refined approach accounting for the irregularity of cellular shapes can be adopted in future studies.

To quantify the invasion of tumor spheroids in the collagen gel matrix in scenario 2, the boundary of each tumor spheroid at $t = 0$ h and $t = 24$ h were defined by thresholding of mCherry signals in ImageJ. The area of the defined boundary was measured in ImageJ. The normalized invasion area of a spheroid was calculated as the difference between the final projected area ($t = 24$ h) and the initial projected area ($t = 0$ h) divided by the initial projected area (Fig. 6Ai).[39,45,83,84,86]

Immunofluorescence staining, confocal imaging, and analysis

After 24 h incubation alone or with N0, N1-like, or N2-like neutrophils in the NTI-chip in scenario 2, PANC-1 tumor spheroids were stained for Ki-67[70] and vimentin[67-69] to assess their levels of proliferation and EMT, respectively. In separate experiments, N0, N1-like, and N2-like neutrophils pre-stained with Vybrant™ DiD dye were stained for typical N1 marker CD54 (ICAM-1) to validate their polarization states at $t = 0$ h and $t = 24$ h in the NTI-chip.[2,19,121] Immunofluorescence staining in the NTI-chip was performed as previously described.[47,116] Briefly, cells were washed with PBS (Gibco) twice and fixed with 4% paraformaldehyde (PFA, Electron Microscopy Sciences) for 15 min at room temperature. The cells were then washed with PBS twice and permeabilized with 0.1% Triton X-100 (Thermo Scientific Chemicals) for 30 min at room temperature. Permeabilization was skipped for staining surface marker CD54 on neutrophils. Cells were washed with PBS twice and blocked with 10% goat serum (Invitrogen, 50062Z) for 2 h at room temperature. To examine tumor spheroid phenotypes, the NTI-chips were incubated overnight at 4 °C with a mixture of mouse anti-Ki-67 (1:500, Invitrogen, 14569980) and rabbit anti-vimentin (1:500, Proteintech, 103661AP) primary antibodies diluted in 10% goat serum. To examine the polarization state of neutrophils, the NTI-chips were incubated overnight at 4 °C with the fluorescently conjugated antibody anti-human CD54-Brilliant Violet 421 (1:100, BioLegend, 353131) diluted in 10% goat serum. The NTI-chips were washed with PBS twice and incubated with PBS for 24 h at 4 °C on a rocker for thorough washing. Tumor spheroids in the NTI-chips were incubated for 10 h at 4 °C with a mixture of the goat anti-mouse Alexa Fluor 488 (1:1000, Invitrogen, A11001) and goat anti-rabbit Alexa Fluor 647 (1:1000, Invitrogen, A21245) secondary antibodies diluted in 10% goat serum. To stain F-actin separately, tumor spheroids in the NTI-chips were incubated for 1 h at room temperature with Alexa Fluor 488 phalloidin (1:400, Invitrogen, A12379) and nuclei stain Hoechst 33342 (1:1000, Thermo Scientific, 62249) diluted in PBS. The NTI-chips were washed with PBS twice and incubated with PBS for 24 h at 4 °C on a rocker for thorough washing. To assess the

end-point apoptosis and overall death of tumor spheroids and neutrophil infiltration after 24 h of time-lapse imaging, the NTI-chips were fixed with 4% PFA for 15 min at room temperature, filled with PBS, and stored at 4 °C in the dark until confocal imaging. To validate the viability of tumor spheroids, the LIVE/DEAD™ Viability/Cytotoxicity Assay Kit (1:2000, Invitrogen, L32250) was added to the NTI-chips after 24 h culture in medium alone or in 5% DMSO as a positive control. All reagents were added to and removed from the NTI-chips through the medium reservoirs in the volume of 100 μL.

The NTI-chips were imaged with a spinning disk confocal microscope (Nikon CSU-W1) using a PLAN APO 10× (NA = 0.45) air objective to capture the viability, overall death, and apoptosis of tumor spheroids and neutrophil infiltration or a 20× (NA = 0.80) air objective to capture F-actin, Ki-67, and vimentin expressions. Z-stacks were acquired at 2 μm intervals using NIS-elements software (AR 5.42.04) and covered a thickness of ~80–120 μm. For tumor spheroids, PANC-1 cancer cells were captured on the mCherry channel, apoptotic cells, Ki-67, or F-actin on the GFP channel, and vimentin on the Cy5 channel. CellTracker BMQC Violet-stained neutrophils or cell nuclei were captured on the DAPI channel.

Tumor spheroid apoptosis was quantified by normalizing the apoptotic volume by the total volume of the spheroid.[91,92] The apoptotic volume of the spheroid was measured based on FITC signals and the total volume of the spheroid based on mCherry signals using the surface function of Imaris 10.2.0 software (Oxford Instruments) (Fig. 7A). FITC signals colocalized with DAPI signals were apoptotic neutrophils and thus excluded from analysis. To quantify neutrophil infiltration per tumor spheroid, the number of neutrophils within the reconstructed spheroid surface was measured based on DAPI signals using the spot function of Imaris.[78] Specifically, the XY diameter of the spots was set to 6.5 μm. An infiltrated neutrophil was defined as a spot whose shortest distance to the reconstructed spheroid surface is lower than 3 μm, including those with negative values[78] (Fig. 5A). Infiltration depth was defined as the absolute value of the shortest distance of an infiltrated neutrophil to the surface of the tumor spheroid. To quantify CD54 expression per neutrophil, the surfaces of DiD-stained neutrophils were created based on Cy5 signals, and the mean intensity of DAPI signals within the reconstructed neutrophil surface was measured. To quantify Ki-67 and vimentin expressions per neutrophil, the surfaces of neutrophils were created based on DAPI signals, and the mean intensities of FITC and Cy5 signals within the reconstructed neutrophil surface were measured respectively. To quantify Ki-67 and vimentin expressions per tumor spheroid, the mean intensities of FITC and Cy5 signals within the spheroid surface created based on mCherry signals were measured respectively. As neutrophils were found to not express Ki-67 but express vimentin (Fig. S10), Cy5 signals co-localized with DAPI signals were vimentin-expressing neutrophils and thus removed from analysis. Imaris was used to create 3D rendering of both

experimental and extracted versions of representative confocal images. ImageJ was used to create representative confocal images using maximum intensity projections of z-stacks and the same brightness and contrast settings were applied to images of all experimental conditions for each channel.

Flow cytometry to confirm marker expressions of neutrophil subtypes

To validate the success of differentiation of HL-60 cells and the polarization of dHL-60 neutrophils, we performed flow cytometry to examine the expression levels of surface markers by each cell type. N0, N1-like, and N2-like dHL-60 neutrophils were collected after polarization to examine expressions of general neutrophil marker CD11b,[74,75] typical N1 markers CD54 (ICAM-1)[high] and CD62L (L-selectin)[low], and typical N2 marker CD182 (CXCR2)[high].[19] HL-60 cells without differentiation were also collected to examine CD11b expression as a negative control. All cells were washed with PBS once and stained with Zombie R685™ Fixable Viability Kit (BioLegend, 423119) to label dead cells for 15 min at room temperature. After washing with Flow Cytometry Staining Buffer (Invitrogen, 00422226) once, cells were stained with the corresponding fluorescently conjugated antibodies: anti-human CD11b-Alexa Fluor 488 (1 : 200, BioLegend, 301317), anti-human CD54-Brilliant Violet 421 (1 : 20, BioLegend, 353131), anti-human CD62L-Brilliant Violet 605 (1 : 20, BioLegend, 304833), and anti-human CXCR2-PE (1 : 20, BioLegend, 320706) diluted in the staining buffer for 20 min at 4 °C. After washing with the staining buffer once, cell samples were fixed with 4% PFA for 10 min, resuspended in the staining buffer, and stored at 4 °C in the dark until being analyzed by an LSR Fortessa flow cytometer (BD Biosciences).

Data were analyzed using FlowJo 10.8.1 software (BD Biosciences). For the gating strategy, cells were first gated based on the side scatter area (SSC-A, cell granularity) versus forward scatter area (FSC-A, cell size) density plot to exclude debris. Single cells were then gated based on the forward scatter height (FSC-H) versus forward scatter area (FSC-A) density plot to exclude cell doublets. Live cells were then gated based on their negative staining for the zombie dye to exclude dead cells.

Reactive oxygen species (ROS) production assay

After polarization, N0, N1-like, and N2-like dHL-60 neutrophils were seeded on a V-bottom 96-well plate at a concentration of 10^6 cells per mL in 100 μL of complete IMDM and treated with 200 nM phorbol 12-myristate 13-acetate (PMA) (Sigma-Aldrich, P8139) to induce ROS production or with DMSO vehicle control in 100 μL for 30 min at 37 °C with 5% CO_2. Dihydrorhodamine 123 (DHR 123) (Invitrogen, D23806) at 1 μM was pre-added to the mixture to stain ROS. Cells were then incubated for 10 min at 4 °C to stop the reaction.[122] After washing with Flow Cytometry Staining Buffer at 4 °C once, cell samples were kept on ice in the dark and analyzed by a LSR Fortessa flow

cytometer immediately. The median fluorescence intensity (MFI) on the FITC channel was measured in FlowJo to represent the level of ROS production.

Neutrophil extracellular trap (NET) release assay

After polarization, N0, N1-like, and N2-like dHL-60 neutrophils were incubated with nuclei stain Hoechst 33342 (1 : 1000, Thermo Scientific, 62249) diluted in complete IMDM on a rotator at 37 °C for 10 min and washed with complete IMDM once. Cells were then seeded on a glass-bottom 96-well plate (Cellvis, P961.5HN) at a concentration of 8×10^5 cells per mL in 100 μL of complete IMDM and treated with 50 nM PMA to induce NET release or with DMSO vehicle control in 100 μL. SYTOX Green (Invitrogen, S7020) at 100 nM was pre-added to the mixture to stain extracellular DNA as a component of NETs.[13,123] Time-lapse imaging was performed on a fully automated Nikon ECLIPSE Ti2-E microscope using a Plan Apo 20× objective (NA = 0.80) at 37 °C with 5% CO_2 to capture NET release over 6 h. Images were acquired using NIS-elements (Nikon Inc.) software and recorded using DAPI (dHL-60 neutrophils) and FITC (NETs) channels at 1 h intervals. Image analysis was performed in ImageJ. NET release was quantified as the percentage of NET-releasing cells per image, i.e., the number of NETs divided by the total number of cells per image. The number of NETs was measured based on FITC signals using Thresholding and Analyze Particles functions. Only objects with a larger area than 13 μm² were classified as NETs. The total number of cells was measured based on DAPI signals using the TrackMate plugin.

Neutrophil cytotoxicity assay in 2D monolayers

To validate the anti-tumor nature of N1-like neutrophils, neutrophil cytotoxicity against PANC-1 cancer cells was assessed in 2D monolayer co-cultures. PANC-1 cancer cells from passages 4 to 14 were seeded on a glass-bottom 96-well plate at a concentration of 10^5 cells per mL in 100 μL of complete IMDM and incubated at 37 °C with 5% CO_2 for 24 h. After media removal from the wells, N0, N1-like, or N2-like neutrophils were added at a concentration of 2×10^6 cells per mL in 100 μL of complete IMDM to the cancer cells to form co-cultures. Complete IMDM containing 5% DMSO was added where applicable as a positive control for cytotoxicity. CellEvent™Caspase-3/7 Green at 2 μM was added to all conditions to stain apoptotic cells. After 24 h incubation at 37 °C with 5% CO_2, the cells were imaged on a Nikon ECLIPSE Ti2-E microscope using a Plan Apo 20× objective (NA = 0.80) to capture apoptosis. Images were acquired using NIS-elements software and recorded using FITC (apoptotic cells) and mCherry (cancer cells) channels. Image analysis was performed in ImageJ. Neutrophil cytotoxicity was quantified as the percentage of apoptotic cancer cells per image, i.e., the number of apoptotic cancer cells divided by the percentage of RFP fluorescence area occupied by all cancer cells. A size filter of 50 μm² to infinity was applied in

the Analyze Particles function to exclude apoptotic neutrophils and debris.

IL-8 secretion assay *via* enzyme-linked immunosorbent assay (ELISA)

The secretion levels of IL-8 by different neutrophil subtypes and by tumor spheroids were examined using ELISA. The supernatants or conditioned media from N0, N1-like, and N2-like dHL-60 neutrophils were collected after 24 h polarization. The supernatant of PANC-1 tumor spheroids was collected from the ULA six-well plate on day 2 of spheroid culture. All supernatants were centrifuged at 2000 × *g* for 10 min at 4 °C to remove cellular debris. All supernatants were frozen at −80 °C for up to one month until analyzed. Concentrations of IL-8 in supernatants were measured using the human IL-8 ELISA kit (BioLegend, 431507) according to the manufacturer's protocol. Samples were tested in triplicate or duplicate without dilution. A microplate reader (BioTek Epoch 2) was used to read the absorbance at 450 nm. Prism 9 software (GraphPad) was used to generate standard curves using the Richard's five-parameter logistic equation and perform data interpolation.

Statistical analysis

All experiments were performed and replicated independently at least three times, unless otherwise stated. Statistical analysis was performed using Prism 9 software (GraphPad). Data were expressed as means ± standard deviations (SD) as indicated. All statistical tests used for the experiments can be found in the corresponding figure legends. A Kruskal–Wallis test or a Mann–Whitney test was used when the data did not pass the Shapiro–Wilk normality test; otherwise, ANOVA or an unpaired t test was used. Differences were considered statistically significant for $p < 0.05$.

Author contributions

Shuai Shao and Caroline N. Jones conceived and designed the experiments. Shuai Shao and Daniel Duncko performed the experiments and data analysis. Shuai Shao, Daniel Duncko, and Caroline N. Jones wrote the manuscript.

Conflicts of interest

There are no conflicts to declare.

Data availability

Supplementary information is available. See DOI: https://doi.org/10.1039/D5LC00526D.

Data for this paper are available at the UT Southwestern Research Data Repository at https://doi.org/10.18738/T8/HQYJ2Y.

Acknowledgements

References

1 B. Lakshmi Narendra, K. Eshvendar Reddy, S. Shantikumar and S. Ramakrishna, Immune system: A double-edged sword in cancer, *Inflammation Res.*, 2013, **62**(9), 823–834, DOI: **10.1007/s00011-013-0645-9**.

2 S. Jaillon, A. Ponzetta, D. Di Mitri, A. Santoni, R. Bonecchi and A. Mantovani, Neutrophil diversity and plasticity in tumour progression and therapy [Internet], *Nat. Rev. Cancer*, 2020, **20**, 485–503, DOI: **10.1038/s41568-020-0281-y**.

3 M. E. Shaul and Z. G. Fridlender, Tumour-associated neutrophils in patients with cancer [Internet], *Nat. Rev. Clin. Oncol.*, 2019, **16**, 601–620, DOI: **10.1038/s41571-019-0222-4**.

4 T. Németh, M. Sperandio and A. Mócsai, Neutrophils as emerging therapeutic targets [Internet], *Nat. Rev. Drug Discovery*, 2020, **19**, 253–275, Available from: **https://www.nature.com/articles/s41573-019-0054-z**.

5 C. C. Hedrick and I. Malanchi, Neutrophils in cancer: heterogeneous and multifaceted [Internet], *Nat. Rev. Immunol.*, 2022, **22**, 173–187, Available from: **https://www.nature.com/articles/s41577-021-00571-6**.

6 R. W. Jenkins, D. A. Barbie and K. T. Flaherty, Mechanisms of resistance to immune checkpoint inhibitors, *Br. J. Cancer*, 2018, **118**(1), 9–16, DOI: **10.1038/bjc.2017.434**.

7 D. Schizas, N. Charalampakis, C. Kole, P. Economopoulou, E. Koustas and E. Gkotsis, *et al.*, Immunotherapy for pancreatic cancer: A 2020 update, *Cancer Treat. Rev.*, 2020, **86**, 102016, DOI: **10.1016/j.ctrv.2020.102016**.

8 S. E. Shelton, H. T. Nguyen, D. A. Barbie and R. D. Kamm, Engineering approaches for studying immune-tumor cell interactions and immunotherapy, *iScience*, 2021, **24**(1), 101985, DOI: **10.1016/j.isci.2020.101985**.

9 R. C. Sterner and R. M. Sterner, CAR-T cell therapy: current limitations and potential strategies [Internet], *Blood Cancer J.*, 2021, **11**, 69, DOI: **10.1038/s41408-021-00459-7**.

10 S. R. Nielsen, J. E. Strøbech, E. R. Horton, R. Jackstadt, A. Laitala and M. C. Bravo, *et al.*, Suppression of tumor-

associated neutrophils by lorlatinib attenuates pancreatic cancer growth and improves treatment with immune checkpoint blockade, *Nat. Commun.*, 2021, **12**(1), 3414, DOI: **10.1038/s41467-021-23731-7**.

11 S. SenGupta, L. E. Hein and C. A. Parent, The Recruitment of Neutrophils to the Tumor Microenvironment Is Regulated by Multiple Mediators [Internet], *Front. Immunol.*, 2021, **12**, 734188, DOI: **10.3389/fimmu.2021.734188**.

12 A. Teijeira, S. Garasa, M. C. Ochoa, M. Villalba, I. Olivera and A. Cirella, *et al.*, IL8, neutrophils, and NETs in a collusion against cancer immunity and immunotherapy, *Clin. Cancer Res.*, 2021, **27**, 2383–2393.

13 Á. Teijeira, S. Garasa, M. Gato, C. Alfaro, I. Migueliz and A. Cirella, *et al.*, CXCR1 and CXCR2 Chemokine Receptor Agonists Produced by Tumors Induce Neutrophil Extracellular Traps that Interfere with Immune Cytotoxicity, *Immunity*, 2020, **52**(5), 856–871.e8.

14 L. Jin, H. S. Kim and J. Shi, Neutrophil in the pancreatic tumor microenvironment [Internet], *Biomolecules*, 2021, **11**, 1170, DOI: **10.3390/biom11081170**.

15 Z. G. Fridlender, J. Sun, S. Kim, V. Kapoor, G. Cheng and L. Ling, *et al.*, Polarization of Tumor-Associated Neutrophil Phenotype by TGF-β: 'N1' versus 'N2' TAN, *Cancer Cell*, 2009, **16**(3), 183–194, Available from: **https://www.cell.com/article/S1535610809002153/fulltext**.

16 J. Jablonska, S. Leschner, K. Westphal, S. Lienenklaus and S. Weiss, Neutrophils responsive to endogenous IFN-β regulate tumor angiogenesis and growth in a mouse tumor model, *J. Clin. Invest.*, 2010, **120**(4), 1151–1164, DOI: **10.1172/JCI37223**.

17 L. Andzinski, N. Kasnitz, S. Stahnke, C. F. Wu, M. Gereke and M. Von Köckritz-Blickwede, *et al.*, Type i IFNs induce anti-tumor polarization of tumor associated neutrophils in mice and human, *Int. J. Cancer*, 2016, **138**(8), 1982–1993.

18 J. Jablonska, C. F. Wu, L. Andzinski, S. Leschner and S. Weiss, CXCR2-mediated tumor-associated neutrophil recruitment is regulated by IFN-β, *Int. J. Cancer*, 2014, **134**(6), 1346–1358, DOI: **10.1002/ijc.28551**.

19 M. Ohms, S. Möller and T. Laskay, An Attempt to Polarize Human Neutrophils Toward N1 and N2 Phenotypes in vitro, *Front. Immunol.*, 2020, **11**, 532, DOI: **10.3389/fimmu.2020.00532**.

20 B. B. Antuamwine, R. Bosnjakovic, F. Hofmann-Vega, X. Wang, T. Theodosiou and I. Iliopoulos, *et al.*, N1 versus N2 and PMN-MDSC: A critical appraisal of current concepts on tumor-associated neutrophils and new directions for human oncology, *Immunol. Rev.*, 2023, **314**(1), 250–279.

21 M. A. Giese, L. E. Hind and A. Huttenlocher, Neutrophil plasticity in the tumor microenvironment, *Blood*, 2019, **133**(20), 2159–2167.

22 Y. Jin, E. S. Christenson, L. Zheng and K. Li, Neutrophils in pancreatic ductal adenocarcinoma: bridging preclinical insights to clinical prospects for improved therapeutic strategies, *Expert Rev. Clin. Immunol.*, 2024, 945–958, DOI: **10.1080/1744666X.2024.2348605**.

23 S. Popescu, M. A. Publik and B. M. Preda, A novel neutrophil-like in vitro model for the study of human neutrophil polarization, *Atherosclerosis*, 2022, **355**, 51, Available from: **https://www.atherosclerosis-journal.com/article/S0021915022006669/fulltext**.

24 Z. Li, Y. Lin, S. Zhang, L. Zhou, G. Yan and Y. Wang, *et al.*, Emodin regulates neutrophil phenotypes to prevent hypercoagulation and lung carcinogenesis, *J. Transl. Med.*, 2019, **17**(1), 1–15, Available from: **https://translational-medicine.biomedcentral.com/articles/10.1186/s12967-019-1838-y**.

25 S. Zhang, L. Zhou, M. Zhang, Y. Wang, M. Wang and J. Du, *et al.*, Berberine maintains the neutrophil N1 phenotype to reverse cancer cell resistance to doxorubicin, *Front. Pharmacol.*, 2020, **10**, 510331.

26 Z. Guo, *Lipocalin-2 Mediated Polarization of Neutrophil in Cerebral Ischemia-Reperfusion Injury*, 2021.

27 X. Zhou, M. Qu, P. Tebon, X. Jiang, C. Wang and Y. Xue, *et al.*, Screening Cancer Immunotherapy: When Engineering Approaches Meet Artificial Intelligence, *Adv. Sci.*, 2020, **7**, 2001447, DOI: **10.1002/advs.202001447**.

28 S. Parlato, G. Grisanti, G. Sinibaldi, G. Peruzzi, C. M. Casciola and L. Gabriele, Tumor-on-a-chip platforms to study cancer-immune system crosstalk in the era of immunotherapy, *Lab Chip*, 2021, **21**, 234–253.

29 K. Paterson, S. Zanivan, R. Glasspool, S. B. Coffelt and M. Zagnoni, Microfluidic technologies for immunotherapy studies on solid tumours, *Lab Chip*, 2021, **21**, 2306–2329.

30 Y. Peng and E. Lee, Microphysiological Systems for Cancer Immunotherapy Research and Development, *Adv. Biol.*, 2024, **8**(8), 2300077, DOI: **10.1002/adbi.202300077**.

31 F. Moresi, F. Noto, J. Vasudevan, X. Bisteau, G. Adriani and A. Pavesi, Microphysiological Systems in Cancer Research: Advancing Immunotherapy through Tumor Microenvironment-Integrated Organ-On-Chip Models [Internet], *Adv. Ther.*, 2025, e00098, DOI: **10.1002/adtp.202500098**.

32 A. Deipenbrock, B. E. Wilmes, T. Sommermann, N. Abdo, K. Moustakas and M. Raasch, *et al.*, Modelling of the multicellular tumor microenvironment of pancreatic ductal adenocarcinoma (PDAC) on a fit-for-purpose biochip for preclinical drug discovery, *Lab Chip*, 2025, **25**(9), 2168–2181, Available from: **https://pubs.rsc.org/en/content/articlehtml/2025/lc/d4lc01016g**.

33 M. F. Harter, T. Recaldin and N. Gjorevski, Organoids as models of immune-organ interaction, *Cell Rep.*, 2025, **44**(9), 116214, Available from: **https://www.sciencedirect.com/science/article/pii/S2211124725009854**.

34 V. Kumar and S. Varghese, Ex Vivo Tumor-on-a-Chip Platforms to Study Intercellular Interactions within the Tumor Microenvironment, *Adv. Healthcare Mater.*, 2019, **8**(4), 1–12.

35 B. A. Yang, T. M. Westerhof, K. Sabin, S. D. Merajver and C. A. Aguilar, Engineered Tools to Study Intercellular Communication, *Adv. Sci.*, 2021, **8**(3), 1–20.

36 D. Irimia and X. Wang, Inflammation-on-a-Chip: Probing the Immune System Ex Vivo [Internet], *Trends Biotechnol.*, 2018, **36**, 923–937.

37 C. N. Jones, J. Dalli, L. Dimisko, E. Wong, C. N. Serhan and D. Irimia, Microfluidic chambers for monitoring leukocyte trafficking and humanized nano-proresolving medicines interactions, *Proc. Natl. Acad. Sci. U. S. A.*, 2012, **109**(50), 20560–20565, DOI: 10.1073/pnas.1210269109.

38 J. Yu, A. Piazza, S. Sparks, L. E. Hind, D. J. Niles and P. N. Ingram, *et al.*, A reconfigurable microscale assay enables insights into cancer-associated fibroblast modulation of immune cell recruitment, *Integr. Biol.*, 2021, **13**(4), 87–97.

39 V. Surendran, D. Rutledge, R. Colmon and A. Chandrasekaran, A novel tumor-immune microenvironment (TIME)-on-Chip mimics three dimensional neutrophil-tumor dynamics and neutrophil extracellular traps (NETs)-mediated collective tumor invasion, *Biofabrication*, 2021, **13**(3), 035029, DOI: 10.1088/1758-5090/abe1cf.

40 J. Park, S. Park, K. A. Hyun and H. I. Jung, Microfluidic recapitulation of circulating tumor cell–neutrophil clusters via double spiral channel-induced deterministic encapsulation, *Lab Chip*, 2021, 3483–3497, DOI: 10.1039/d1lc00433f.

41 M. B. Chen, C. Hajal, D. C. Benjamin, C. Yu, H. Azizgolshani and R. O. Hynes, *et al.*, Inflamed neutrophils sequestered at entrapped tumor cells via chemotactic confinement promote tumor cell extravasation, *Proc. Natl. Acad. Sci. U. S. A.*, 2018, **115**(27), 7022–7027, DOI: 10.1073/pnas.1715932115.

42 A. Spiegel, M. W. Brooks, S. Houshyar, F. Reinhardt, M. Ardolino and E. Fessler, *et al.*, Neutrophils suppress intraluminal NK cell-mediated tumor cell clearance and enhance extravasation of disseminated carcinoma cells, *Cancer Discovery*, 2016, **6**(6), 630–649.

43 M. Crippa, G. Talò, A. Lamouline, S. Bolis, C. Arrigoni and S. Bersini, *et al.*, A microfluidic model of human vascularized breast cancer metastasis to bone for the study of neutrophil-cancer cell interactions, *Mater. Today Bio*, 2022, **17**, 100460, DOI: 10.1016/j.mtbio.2022.100460.

44 M. Crippa, S. Bersini, M. Gilardi, C. Arrigoni, S. Gamba and A. Falanga, *et al.*, A microphysiological early metastatic niche on a chip reveals how heterotypic cell interactions and inhibition of integrin subunit β3 impact breast cancer cell extravasation, *Lab Chip*, 2021, **21**(6), 1061–1072, Available from: https://pubs.rsc.org/en/content/articlehtml/2021/lc/d0lc01011a.

45 S. Safarulla, A. Madan, F. Xing and A. Chandrasekaran, CXCR2 Mediates Distinct Neutrophil Behavior in Brain Metastatic Breast Tumor, *Cancers*, 2022, **14**(3), 515, DOI: 10.3390/cancers14030515.

46 E. Kromidas, A. Geier, A. Weghofer, H. Liu, M. Weiß and P. Loskill, Immunocompetent PDMS-free Organ-on-Chip Model of Cervical Cancer Integrating Patient-Specific Cervical Fibroblasts and Neutrophils, *Adv. Healthcare Mater.*, 2023, 2302714.

47 S. Shao, N. A. Delk and C. N. Jones, A microphysiological system reveals neutrophil contact-dependent attenuation of pancreatic tumor progression by CXCR2 inhibition-based immunotherapy, *Sci. Rep.*, 2024, **14**(1), 1–16, Available from: https://www.nature.com/articles/s41598-024-64780-4.

48 P. Xu, J. Chi, X. Wang, M. Zhu, K. Chen and Q. Fan, *et al.*, In vitro vascularized liver tumor model based on a microfluidic inverse opal scaffold for immune cell recruitment investigation, *Lab Chip*, 2024, **24**, 3470–3479, DOI: 10.1039/d4lc00341a.

49 K. A. Babatunde, R. Datta, N. W. Hendrikse, J. M. Ayuso, A. Huttenlocher and M. C. Skala, *et al.*, Naive primary neutrophils play a dual role in the tumor microenvironment, *iScience*, 2024, **27**(9), 110632, Available from: https://www.cell.com/article/S2589004224018571/fulltext.

50 S. Parlato, A. De Ninno, R. Molfetta, E. Toschi, D. Salerno and A. Mencattini, *et al.*, 3D Microfluidic model for evaluating immunotherapy efficacy by tracking dendritic cell behaviour toward tumor cells, *Sci. Rep.*, 2017, **7**(1), 1–16.

51 M. Nguyen, A. De Ninno, A. Mencattini, F. Mermet-Meillon, G. Fornabaio and S. S. Evans, *et al.*, Dissecting Effects of Anti-cancer Drugs and Cancer-Associated Fibroblasts by On-Chip Reconstitution of Immunocompetent Tumor Microenvironments, *Cell Rep.*, 2018, **25**(13), 3884–3893.e3.

52 A. Mencattini, A. De Ninno, J. Mancini, L. Businaro, E. Martinelli and G. Schiavoni, *et al.*, High-throughput analysis of cell-cell crosstalk in ad hoc designed microfluidic chips for oncoimmunology applications, *Methods Enzymol.*, 2020, 479–502, DOI: 10.1016/bs.mie.2019.06.012.

53 A. De Ninno, F. R. Bertani, A. Gerardino, G. Schiavoni, M. Musella and C. Galassi, *et al.*, Microfluidic co-culture models for dissecting the immune response in in vitro tumor microenvironments, *J. Visualized Exp.*, 2021, **2021**(170), 61895.

54 A. Mencattini, C. Lansche, I. Veith, P. Erbs, J. M. Balloul and E. Quemeneur, *et al.*, Direct imaging and automatic analysis in tumor-on-chip reveal cooperative antitumoral activity of immune cells and oncolytic vaccinia virus, *Biosens. Bioelectron.*, 2022, **215**, 114571.

55 I. Veith, M. Nurmik, A. Mencattini, I. Damei, C. Lansche and S. Brosseau, *et al.*, Assessing personalized responses to anti-PD-1 treatment using patient-derived lung tumor-on-chip, *Cell Rep. Med.*, 2024, **5**(5), 101549, DOI: 10.1016/j.xcrm.2024.101549.

56 Z. Ao, H. Cai, Z. Wu, L. Hu, A. Nunez and Z. Zhou, *et al.*, Microfluidics guided by deep learning for cancer immunotherapy screening, *Proc. Natl. Acad. Sci. U. S. A.*, 2022, **119**(46), e2214569119, DOI: 10.1073/pnas.2214569119.

57 Y. Cho, M. S. Laird, T. Bishop, R. Li, D. Jazwinska and E. Ruffo, *et al.*, CAR T cell infiltration and cytotoxic killing within the core of 3D breast cancer spheroids under the control of antigen sensing in microwell arrays, *APL Bioeng.*, 2024, **8**(3), 36105, DOI: 10.1063/5.0207941.

58 C. Ma, H. Wang, L. Liu, R. Chen, N. Mukherjee and J. Tong, *et al.*, Bioengineered immunocompetent preclinical trial-on-chip tool enables screening of CAR T cell therapy for leukaemia, *Nat. Biomed. Eng.*, 2025, 1–17, Available from: https://www.nature.com/articles/s41551-025-01428-2.

59 A. R. Aref, R. Y. J. Huang, W. Yu, K. N. Chua, W. Sun and T. Y. Tu, et al., Screening therapeutic EMT blocking agents in a three-dimensional microenvironment, Integr. Biol., 2013, 5(2), 381.

60 H. Ungefroren, I. Thürling, B. Färber, T. Kowalke, T. Fischer and L. V. M. De Assis, et al., The Quasimesenchymal Pancreatic Ductal Epithelial Cell Line PANC-1—A Useful Model to Study Clonal Heterogeneity and EMT Subtype Shifting, Cancers, 2022, 14(9), 2057, Available from: https://www.mdpi.com/2072-6694/14/9/2057/htm.

61 E. Tomás-Bort, M. Kieler, S. Sharma, J. B. Candido and D. Loessner, 3D approaches to model the tumor microenvironment of pancreatic cancer, Theranostics, 2020, 10(11), 5074–5089.

62 C. Tian, K. R. Clauser, D. Öhlund, S. Rickelt, Y. Huang and M. Gupta, et al., Proteomic analyses of ECM during pancreatic ductal adenocarcinoma progression reveal different contributions by tumor and stromal cells, Proc. Natl. Acad. Sci. U. S. A., 2019, 116(39), 19609–19618, DOI: 10.1073/pnas.1908626116.

63 T. J. Puls, X. Tan, C. F. Whittington and S. L. Voytik-Harbin, 3D collagen fibrillar microstructure guides pancreatic cancer cell phenotype and serves as a critical design parameter for phenotypic models of EMT, PLoS One, 2017, 12(11), e0188870, DOI: 10.1371/journal.pone.0188870.

64 V. S. Shirure, S. Yechikov, B. S. Shergill, T. Dehghani, A. V. Block and H. Sodhi, et al., Mitigating neutrophil trafficking and cardiotoxicity with DS–IkL in a microphysiological system of a cytokine storm, Lab Chip, 2023, 23, 3050–3061, DOI: 10.1039/d2lc01070d.

65 Y. Bi, V. S. Shirure, R. Liu, C. Cunningham, L. Ding and J. M. Meacham, et al., Tumor-on-a-chip platform to interrogate the role of macrophages in tumor progression, Integr. Biol., 2020, 12(9), 221–232.

66 R. S. Bains, T. G. Raju, L. C. Semaan, A. Block, Y. Yamaguchi and S. J. Priceman, et al., Vascularized tumor-on-a-chip to investigate immunosuppression of CAR-T cells, Lab Chip, 2025, 25, 2390–2400, DOI: 10.1039/d4lc01089b.

67 Y. Shichi, N. Sasaki, M. Michishita, F. Hasegawa, Y. Matsuda and T. Arai, et al., Enhanced morphological and functional differences of pancreatic cancer with epithelial or mesenchymal characteristics in 3D culture, Sci. Rep., 2019, 9(1), 1–10, Available from: https://www.nature.com/articles/s41598-019-47416-w.

68 J. H. Lee, S. K. Kim, I. A. Khawar, S. Y. Jeong, S. Chung and H. J. Kuh, Microfluidic co-culture of pancreatic tumor spheroids with stellate cells as a novel 3D model for investigation of stroma-mediated cell motility and drug resistance, J. Exp. Clin. Cancer Res., 2018, 37, 4, DOI: 10.1186/s13046-017-0654-6.

69 S. K. Kim, S. D. Jang, H. Kim, S. Chung, J. K. Park and H. J. Kuh, Phenotypic heterogeneity and plasticity of cancer cell migration in a pancreatic tumor three-dimensional culture model, Cancers, 2020, 12(5), 1305, Available from: https://www.mdpi.com/2072-6694/12/5/1305.

70 N. Menon, H. X. Dang, U. S. Datla, M. Moarefian, C. B. Lawrence and C. A. Maher, et al., Heparin-based hydrogel scaffolding alters the transcriptomic profile and increases the chemoresistance of MDA-MB-231 triple-negative breast cancer cells, Biomater. Sci., 2020, 8(10), 2786–2796.

71 V. S. Shirure, C. C. W. Hughes and S. C. George, Engineering Vascularized Organoid-on-a-Chip Models, Annu. Rev. Biomed. Eng., 2021, 6, 293–312, DOI: 10.1146/annurev-bioeng-090120-094330.

72 M. Baggiolini and I. Clark-Lewis, Interleukin-8, a chemotactic and inflammatory cytokine, FEBS Lett., 1992, 307(1), 97–101.

73 B. P. Boribong, M. J. Lenzi, L. Li and C. N. Jones, Super-low dose lipopolysaccharide dysregulates neutrophil migratory decision-making, Front. Immunol., 2019, 10, 1–12.

74 E. Rincón, B. L. Rocha-Gregg and S. R. Collins, A map of gene expression in neutrophil-like cell lines, BMC Genomics, 2018, 19, 573, DOI: 10.1186/s12864-018-4957-6.

75 Y. Guo, F. Gao, Q. Wang, K. Wang, S. Pan and Z. Pan, et al., Differentiation of HL-60 cells in serum-free hematopoietic cell media enhances the production of neutrophil extracellular traps, Exp. Ther. Med., 2021, 21(4), 353, DOI: 10.3892/etm.2021.9784.

76 S. Fujishima, A. R. Hoffman, T. Vu, K. J. Kim, H. Zheng and D. Daniel, et al., Regulation of neutrophil interleukin 8 gene expression and protein secretion by LPS, TNF-α, and IL-1β, J. Cell. Physiol., 1993, 154(3), 478–485.

77 M. van Egmond, Neutrophils in antibody-based immunotherapy of cancer, Expert Opin. Biol. Ther., 2008, 8(1), 83–94.

78 T. I. Maulana, C. Teufel, M. Cipriano, J. Roosz, L. Lazarevski and F. E. van den Hil, et al., Breast cancer-on-chip for patient-specific efficacy and safety testing of CAR-T cells, Cell Stem Cell, 2024, 31, 1–14, DOI: 10.1016/j.stem.2024.04.018.

79 S. Tazzyman, S. T. Barry, S. Ashton, P. Wood, D. Blakey and C. E. Lewis, et al., Inhibition of neutrophil infiltration into A549 lung tumors in vitro and in vivo using a CXCR2-specific antagonist is associated with reduced tumor growth, Int. J. Cancer, 2011, 129(4), 847–858.

80 Z. Du, S. Mi, X. Yi, Y. Xu and W. Sun, Microfluidic system for modelling 3D tumour invasion into surrounding stroma and drug screening, Biofabrication, 2018, 10(3), 034102, DOI: 10.1088/1758-5090/aac70c.

81 Y. L. Huang, Y. Ma, C. Wu, C. Shiau, J. E. Segall and M. Wu, Tumor spheroids under perfusion within a 3D microfluidic platform reveal critical roles of cell-cell adhesion in tumor invasion, Sci. Rep., 2020, 10(1), 9648, DOI: 10.1038/s41598-020-66528-2.

82 T. N. Seyfried and L. C. Huysentruyt, On the origin of cancer metastasis, Crit. Rev. Oncog., 2013, 18(1–2), 43–73.

83 D. Pally, M. Banerjee, S. Hussain, R. V. Kumar, A. Petersson and E. Rosendal, et al., Galectin-9 Signaling Drives Breast Cancer Invasion through Extracellular Matrix, ACS Chem. Biol., 2022, 17(6), 1376–1386, DOI: 10.1021/acschembio.1c00902.

84 M. Vinci, C. Box and S. A. Eccles, Three-dimensional (3D) tumor spheroid invasion assay, J. Visualized Exp., 2015, 2015(99), e52686, Available from: https://www.jove.com/v/52686/three-dimensional-3d-tumor-spheroid-invasion-assay.

85 A. A. Shimpi, M. L. Tan, M. Vilkhovoy, D. Dai, L. D. M. Roberts and J. C. H. Kuo, et al., Convergent Approaches to Delineate the Metabolic Regulation of Tumor Invasion by Hyaluronic Acid Biosynthesis, Adv. Healthcare Mater., 2022, 12, 2202224, DOI: 10.1002/adhm.202202224.

86 I. S. Chan, H. Knutsdóttir, G. Ramakrishnan, V. Padmanaban, M. Warrier and J. C. Ramirez, et al., Cancer cells educate natural killer cells to a metastasis-promoting cell state, J. Cell Biol., 2020, 219(9), e202001134, DOI: 10.1083/jcb.202001134.

87 F. Carnevali, S. Forciniti, V. Onesto, A. C. Siciliano, H. Iuele and G. Grasso, et al., Advancements in Cancer Research: 3D Models, Single-Cell, and Live-Cell Techniques for Better Insights, Adv. Ther., 2024, 2400351.

88 M. S. F. Ng, I. Kwok, L. Tan, C. Shi, D. Cerezo-Wallis and Y. Tan, et al., Deterministic reprogramming of neutrophils within tumors, Science, 2024, 383(6679), eadf6493, Available from: https://www.ncbi.nlm.nih.gov/pubmed/38207030.

89 A. R. Aref, M. Campisi, E. Ivanova, A. Portell, D. Larios and B. P. Piel, et al., 3D microfluidic: Ex vivo culture of organotypic tumor spheroids to model immune checkpoint blockade, Lab Chip, 2018, 18(20), 3129–3143.

90 R. W. Jenkins, A. R. Aref, P. H. Lizotte, E. Ivanova, S. Stinson and C. W. Zhou, et al., Ex vivo profiling of PD-1 blockade using organotypic tumor spheroids, Cancer Discovery, 2018, 8(2), 196–215.

91 S. W. L. Lee, G. Adriani, E. Ceccarello, A. Pavesi, A. T. Tan and A. Bertoletti, et al., Characterizing the role of monocytes in T cell cancer immunotherapy using a 3d microfluidic model, Front. Immunol., 2018, 9, 6, DOI: 10.3389/fimmu.2018.00416.

92 A. Pavesi, A. T. Tan, S. Koh, A. Chia, M. Colombo and E. Antonecchia, et al., A 3D microfluidic model for preclinical evaluation of TCR-engineered T cells against solid tumors, JCI Insight, 2017, 2(12), e89762, DOI: 10.1172/jci.insight.89762.

93 E. Yildiz-Ozturk and O. Yesil-Celiktas, Diffusion phenomena of cells and biomolecules in microfluidic devices, Biomicrofluidics, 2015, 9(5), 1–18, DOI: 10.1063/1.4923263.

94 R. Tran, D. R. Myers, G. Denning, J. E. Shields, A. M. Lytle and H. Alrowais, et al., Microfluidic Transduction Harnesses Mass Transport Principles to Enhance Gene Transfer Efficiency, Mol. Ther., 2017, 25(10), 2372–2382, Available from: https://www.cell.com/article/S1525001617303167/fulltext.

95 C. N. Jones, L. Dimisko, K. Forrest, K. Judice, M. C. Poznansky and J. F. Markmann, et al., Human neutrophils are primed by chemoattractant gradients for blocking the growth of aspergillus fumigatus, J. Infect. Dis., 2016, 213(3), 465–475, DOI: 10.1093/infdis/jiv419.

96 S. Halldorsson, E. Lucumi, R. Gómez-Sjöberg and R. M. T. Fleming, Advantages and challenges of microfluidic cell culture in polydimethylsiloxane devices, Biosens. Bioelectron., 2015, 63, 218–231.

97 T. P. Brouwer, A. L. Vahrmeijer and N. F. C. C. De Miranda, Immunotherapy for pancreatic cancer: chasing the light at the end of the tunnel, Cell. Oncol., 2021, 44(2), 261–278, DOI: 10.1007/s13402-021-00587-z.

98 I. L. Linde, T. R. Prestwood, J. Qiu, G. Pilarowski, M. H. Linde and X. Zhang, et al., Neutrophil-activating therapy for the treatment of cancer, Cancer Cell, 2023, 41(2), 356–372.e10, Available from: https://www.cell.com/article/S1535610823000028/fulltext.

99 Y. Chang, R. Syahirah, X. Wang, G. Jin, S. Torregrosa-Allen and B. D. Elzey, et al., Engineering chimeric antigen receptor neutrophils from human pluripotent stem cells for targeted cancer immunotherapy, Cell Rep., 2022, 40(3), 111128, DOI: 10.1016/j.celrep.2022.111128.

100 Y. Wu, J. Ma, X. Yang, F. Nan, T. Zhang and S. Ji, et al., Neutrophil profiling illuminates anti-tumor antigen-presenting potency, Cell, 2024, 187(6), 1422–1439.e24, DOI: 10.1016/j.cell.2024.02.005.

101 J. Gungabeesoon, N. A. Gort-Freitas, M. Kiss, E. Bolli, M. Messemaker and M. Siwicki, et al., A neutrophil response linked to tumor control in immunotherapy, Cell, 2023, 186(7), 1448–1464.e20.

102 I. M. Richardson, C. J. Calo, E. L. Ginter, E. Niehaus, K. A. Pacheco and L. E. Hind, Diverse bacteria elicit distinct neutrophil responses in a physiologically relevant model of infection, iScience, 2024, 27(1), 108627, DOI: 10.1016/j.isci.2023.108627.

103 A. C. I. Van Steen, L. Kempers, R. Schoppmeyer, M. Blokker, D. J. Beebe and M. A. Nolte, et al., Transendothelial migration induces differential migration dynamics of leukocytes in tissue matrix, J. Cell Sci., 2021, 134(21), jcs258690, DOI: 10.1242/jcs.258690.

104 Y. Zhao, Y. Wu, K. Islam, R. Paul, Y. Zhou and X. Qin, et al., Microphysiologically Engineered Vessel-Tumor Model to Investigate Vascular Transport Dynamics of Immune Cells, ACS Appl. Mater. Interfaces, 2024, 16(18), 22839–22849, DOI: 10.1021/acsami.4c00391.

105 Z. Wan, M. A. Floryan, M. F. Coughlin, S. Zhang, A. X. Zhong and S. E. Shelton, et al., New Strategy for Promoting Vascularization in Tumor Spheroids in a Microfluidic Assay, Adv. Healthcare Mater., 2023, 12(14), 2201784, DOI: 10.1002/adhm.202201784.

106 Z. Wan, S. Zhang, A. X. Zhong, L. Xu, M. F. Coughlin and G. Pavlou, et al., Transmural Flow Upregulates PD-L1 Expression in Microvascular Networks, Adv. Sci., 2024, 2400921, DOI: 10.1002/advs.202400921.

107 I. K. Zervantonakis, S. K. Hughes-Alford, J. L. Charest, J. S. Condeelis, F. B. Gertler and R. D. Kamm, Three-dimensional microfluidic model for tumor cell intravasation and endothelial barrier function, Proc. Natl. Acad. Sci. U. S. A., 2012, 109(34), 13515–13520.

108 E. N. Tevonian, E. L. Kan, K. K. Maniar, A. J. Wang, A. Datta and R. D. Kamm, et al., A Vascularized Liver Microphysiological System Captures Key Features of Hepatic Insulin Resistance and Monocyte Infiltration, bioRxiv, 2025, preprint, 2025.01.09.632182, DOI: 10.1101/2025.01.09.632182.

109 A. J. McFarlane, F. Fercoq, S. B. Coffelt and L. M. Carlin, Neutrophil dynamics in the tumor microenvironment, J. Clin. Invest., 2021, 131(6), 1–10.

110 J. M. Ayuso, M. Virumbrales-Muñoz, J. M. Lang and D. J. Beebe, A role for microfluidic systems in precision medicine [Internet], *Nat. Commun.*, 2022, **13**, 3086, DOI: **10.1038/s41467-022-30384-7**.

111 S. Deng, C. Li, J. Cao, Z. Cui, J. Du and Z. Fu, *et al.*, Organ-on-a-chip meets artificial intelligence in drug evaluation [Internet], *Theranostics*, 2023, **13**, 4526–4558, DOI: **10.7150/thno.87266**.

112 S. R. Akash, M. A. J. B. Arnob and M. J. Uddin, FDA Modernization Act 2.0: An insight from nondeveloping country [Internet], *Drug Dev. Res.*, 2023, **84**, 1572–1577, DOI: **10.1002/ddr.22108**.

113 U. Marx, S. Beken, Z. Chen, E. M. Dehne, A. Doherty and L. Ewart, *et al.*, Biology-Inspired Dynamic Microphysiological System Approaches to Revolutionize Basic Research, Healthcare and Animal Welfare, *ALTEX*, 2025, **42**(2), 204–223.

114 A. M. Gonzalez-suarez, M. Medlyn, D. Choi, G. Stybayeva, D. D. Billadeau and A. Revzin, Microfluidic Co-Cultures of Cancer Spheroids and NK Cells for Testing Immunotherapy, *2023 22nd International Conference on Solid-State Sensors, Actuators and Microsystems (Transducers)*, Department of Immunology College of Medicine, Mayo Clinic, US, 2023, pp. 654–657.

115 D. Choi, A. M. Gonzalez-Suarez, M. G. Dumbrava, M. Medlyn, J. M. de Hoyos-Vega and F. Cichocki, *et al.*, Microfluidic Organoid Cultures Derived from Pancreatic Cancer Biopsies for Personalized Testing of Chemotherapy and Immunotherapy, *Adv. Sci.*, 2023, 2303088, DOI: **10.1002/advs.202303088**.

116 Y. Shin, S. Han, J. S. Jeon, K. Yamamoto, I. K. Zervantonakis and R. Sudo, *et al.*, Microfluidic assay for simultaneous culture of multiple cell types on surfaces or within hydrogels, *Nat. Protoc.*, 2012, **7**(7), 1247–1259.

117 T. Hu, A. Villarroel, A. Duff, I. Ruiz and A. Almeida, DMSO inhibits growth and induces apoptosis through extrinsic pathway in human cancer cells, *J. Med. Discovery*, 2020, **5**(4), 20055, DOI: **10.24262/jmd.5.4.20055**.

118 A. Pavesi, G. Adriani, A. Tay, M. E. Warkiani, W. H. Yeap and S. C. Wong, *et al.*, Engineering a 3D microfluidic culture platform for tumor-treating field application, *Sci. Rep.*, 2016, **6**, 26584, DOI: **10.1038/srep26584**.

119 D. Ershov, M. S. Phan, J. W. Pylvänäinen, S. U. Rigaud, L. Le Blanc and A. Charles-Orszag, *et al.*, TrackMate 7: integrating state-of-the-art segmentation algorithms into tracking pipelines, *Nat. Methods*, 2022, **19**(7), 829–832, DOI: **10.1038/s41592-022-01507-1**.

120 P. Zengel, A. Nguyen-Hoang, C. Schildhammer, R. Zantl, V. Kahl and E. Horn, μ-Slide Chemotaxis: a new chamber for long-term chemotaxis studies, *BMC Cell Biol.*, 2011, **12**, 21, DOI: **10.1186/1471-2121-12-21**.

121 J. Bai, G. Adriani, T. M. Dang, T. Y. Tu, H. X. L. Penny and S. C. Wong, *et al.*, Contact-dependent carcinoma aggregate dispersion by M2a macrophages via ICAM-1 and ß2 integrin interactions, *Oncotarget*, 2015, **6**(28), 25295–25307, DOI: **10.18632/oncotarget.4716**.

122 Y. Chen and W. G. Junger, Measurement of oxidative burst in neutrophils, *Methods Mol. Biol.*, 2012, **844**, 115–124, DOI: **10.1007/978-1-61779-527-5_8**.

123 U. S. Datla, B. Vundurthy, J. S. Hook, N. Menon, H. Razmi Bagtash and T. Shihabeddin, *et al.*, Quantifying neutrophil extracellular trap release in a combined infection-inflammation NET-array device, *Lab Chip*, 2024, **24**(3), 615–628, Available from: **https://pubs.rsc.org/en/content/articlehtml/2024/lc/d3lc00648d**.